MIT Libraries | DSpace@MIT

MIT Open Access Articles

Reference Array and Design Consideration for the Next-Generation Event Horizon Telescope

Massachusetts Institute of Technology

Article

Reference Array and Design Consideration for the Next-Generation Event Horizon Telescope

Sheperd S. Doeleman [1,2,*], John Barrett [3], Lindy Blackburn [1,2], Katherine L. Bouman [4], Avery E. Broderick [5,6,7], Ryan Chaves [1], Vincent L. Fish [3], Garret Fitzpatrick [1], Mark Freeman [1], Antonio Fuentes [8], José L. Gómez [8], Kari Haworth [1], Janice Houston [1], Sara Issaoun [1,†], Michael D. Johnson [1,2], Mark Kettenis [9], Laurent Loinard [10], Neil Nagar [11], Gopal Narayanan [12], Aaron Oppenheimer [1], Daniel C. M. Palumbo [1,2], Nimesh Patel [1], Dominic W. Pesce [1,2], Alexander W. Raymond [1,13], Freek Roelofs [1,2], Ranjani Srinivasan [1], Paul Tiede [1,2], Jonathan Weintroub [1,2] and Maciek Wielgus [14]

1   Center for Astrophysics|Harvard & Smithsonian, 60 Garden Street, Cambridge, MA 02138, USA
2   Black Hole Initiative, Harvard University, 20 Garden Street, Cambridge, MA 02138, USA
3   Massachusetts Institute of Technology Haystack Observatory, 99 Millstone Road, Westford, MA 01886, USA
4   California Institute of Technology, 1200 East California Boulevard, Pasadena, CA 91125, USA
5   Perimeter Institute for Theoretical Physics, 31 Caroline Street North, Waterloo, ON N2L 2Y5, Canada
6   Department of Physics and Astronomy, University of Waterloo, 200 University Avenue West, Waterloo, ON N2L 3G1, Canada
7   Waterloo Centre for Astrophysics, University of Waterloo, Waterloo, ON N2L 3G1, Canada
8   Instituto de Astrofísica de Andalucía-CSIC, Glorieta de la Astronomía s/n, E-18008 Granada, Spain
9   Joint Institute for VLBI ERIC (JIVE), Oude Hoogeveensedijk 4, 7991 PD Dwingeloo, The Netherlands
10 Instituto de Radioastronomía y Astrofísica, Universidad Nacional Autónoma de México, Morelia 58089, Mexico
11 Astronomy Department, Universidad de Concepción, Casilla 160-C, Concepción 4030000, Chile
12 Department of Astronomy, University of Massachusetts, Amherst, MA 01003, USA; gopal@astro.umass.edu
13 Jet Propulsion Laboratory, California Institute of Technology 4800 Oak Grove Dr., Pasadena, CA 91109, USA
14 Max–Planck–Institut für Radioastronomie, Auf dem Hügel 69, D-53121 Bonn, Germany
*   Correspondence: sdoeleman@cfa.harvard.edu
†   NASA Hubble Fellowship Program, Einstein Fellow.

Abstract: We describe the process to design, architect, and implement a transformative enhancement of the Event Horizon Telescope (EHT). This program—the next-generation Event Horizon Telescope (ngEHT)—will form a networked global array of radio dishes capable of making high-fidelity real-time movies of supermassive black holes (SMBH) and their emanating jets. This builds upon the EHT principally by deploying additional modest-diameter dishes to optimized geographic locations to enhance the current global mm/submm wavelength Very Long Baseline Interferometric (VLBI) array, which has, to date, utilized mostly pre-existing radio telescopes. The ngEHT program further focuses on observing at three frequencies simultaneously for increased sensitivity and Fourier spatial frequency coverage. Here, the concept, science goals, design considerations, station siting, and instrument prototyping are discussed, and a preliminary reference array to be implemented in phases is described.

Keywords: black holes; supermassive black holes; general relativity; interferometry; accretion; relativistic jets; very-long-baseline interferometry; radio instrumentation; EHT; ngEHT

1. Introduction

On 10 April 2019, the Event Horizon Telescope project (EHT) released images of the supermassive black hole at the heart of galaxy M87 [1–6]. The observed ring of emission, formed by radio waves lensed in the gravitational field of a 6.5 billion solar mass black hole, has dimensions that match the predictions of General Relativity. Images of Sgr A*,

the 4 million solar mass black hole at the center of the Milky Way, also exhibit a ring morphology with diameters anticipated by theory [7–12]. These results confirm that the EHT has observed the strong gravitational lensing signature of supermassive black holes [13–17], and these images have opened a new field of precision black hole studies on horizon scales.

This work is built upon decades of technical development and precursor observations. Pioneering first Very Long Baseline Interferometry (VLBI) experiments at wavelengths of 1.3 mm [18,19] demonstrated that observations with the required resolution were possible at frequencies where AGN are likely to be optically thin. The discovery of horizon-scale structure in both Sgr A* and M87 with purpose-built ultra-high bandwidth systems on early EHT arrays [20,21] confirmed that imaging these sources was feasible. Subsequent observations revealed time-variability and ordered magnetic fields on Schwarzschild radius dimensions [22,23]. The emergence of the EHT to a full imaging array grew from building community support through a decadal review processes [24], efforts to modify large-scale international facilities, such as ALMA, through global cooperation [25,26], and work to enable VLBI capability at the most remote observatories on the planet [27,28]. Over the course of two decades, all the technical, logistical, organizational, and analytical aspects of the full EHT were implemented by an expert team that grew from a few 10's to over 200 collaborators worldwide.

Building upon this legacy, the next-generation EHT (ngEHT) provides a roadmap to greatly accelerate the development of the EHT, envisaging a transformative new instrument capable of delivering real-time black hole movies. Where the EHT used existing mm/sub-mm facilities to form the first imaging array, the ngEHT will take the next step by designing and locating new dishes to optimize performance and scientific return. This vision offers excellent opportunities to engage the curious public on many levels. It is estimated that over a billion people have now seen the M87 image [29]. We anticipate that the long-term public and STEM education engagement as the ngEHT builds to its goal of black hole 'cinema' will be similar in scope.

For the purposes of this paper, the term "ngEHT" is used to describe a program to explore and define a long-term plan to enhance the EHT to realize a new set of transformative science goals. This paper describes that vision by outlining improvements in bandwidth, frequency range, new antenna deployment, and new operating modes that enable increases in angular resolution, Fourier spatial frequency coverage, sensitivity, and temporal resolution. For brevity, "ngEHT" will also be used as shorthand for the future arrays that will emerge through these plans, as well as for the constellation of improvements that constitute the ngEHT concept.

Technical advances in several areas make the design and implementation of the ngEHT within this decade a realistic goal. Over most of the past two decades, the bandwidth of VLBI systems has kept pace with Moore's Law—a doubling of capacity and speed approximately every 18 months (see, e.g., Event Horizon Telescope Collaboration et al. [2] and Figure 1 below). This is primarily due to the migration of VLBI instrumentation development to designs that adopt industry-standard components, including CPUs, Analog to Digital Converters, Field Programmable Gate Arrays (FPGA), and commercial data transmission protocols (e.g., Vertatschitsch et al. [30]). The increased bandwidth of these components and systems match the analog bandwidth improvements planned for international and national submm facilities, including ALMA [31] and the Submillimeter Array [32]. Meanwhile, the transport of larger data volumes captured by next-generation VLBI systems can be accommodated either by high-speed internet connections [33,34], or increased capacity of hard disk and solid-state disk, which can be shipped by commercial carriers. Once gathered at a central computing facility, the many 10s of Petabytes anticipated for next-generation EHT array observations can be correlated by purpose-built clusters, allocated time on national super-computing centers, or through virtual machine creation using cloud architectures (e.g., Gill et al. [35]). Once correlated, data analysis options include a growing number of video reconstruction algorithms that can render the dynamics of supermassive

black hole activity on horizon scales [36–38]. These developments, combined with a positive mention of the ngEHT project [39] in the Radio/Millimeter/sub-Milimeter panel of the most recent US Astronomy Decadal Review [40], imply that implementing the ngEHT is both feasible and timely.
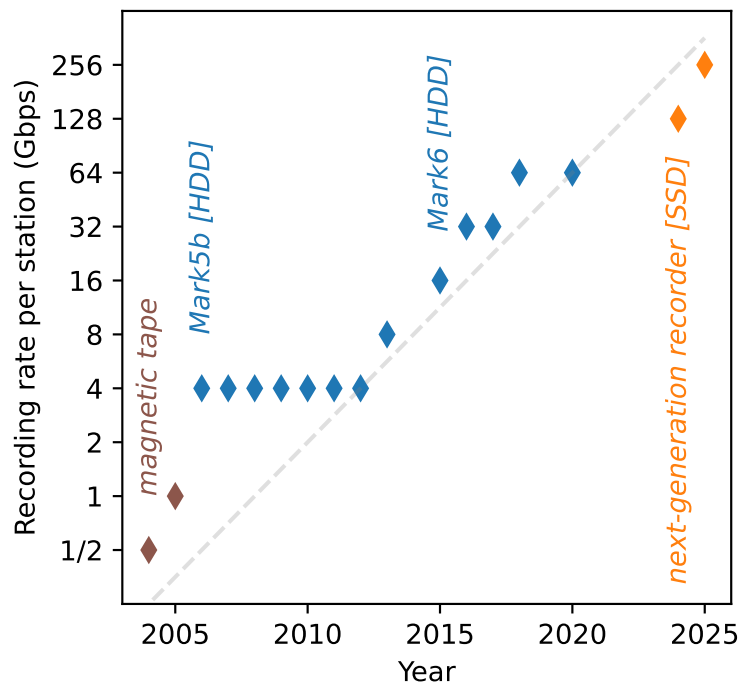
Figure 1. EHT/ngEHT data rate per station over two decades, roughly doubling every two years. The large bandwidths provide the EHT/ngEHT the necessary continuum sensitivity for ultra-high resolution VLBI imaging at (sub-)1 mm using a highly heterogeneous network of telescopes. Maintaining this trend has required the regular adoption of commercial technologies as they became available.

2. ngEHT Concept

The first images of M87 and Sgr A* revealed a clear ring morphology, but they achieved a dynamic range of only ∼10 [4,9]. Image fidelity from the 2017 data sets was primarily limited by sparse interferometric baseline coverage. The shortest baselines, between telescopes located at the same geographic location (ALMA-APEX in Chile and JCMT-SMA in Hawai'i), probe arc second scale structures. There is a large gap between these "intra-site" baselines and the first "inter-site" baseline that links LMT-SMT, which creates a baseline with an angular resolution corresponding to ∼150 µas. Furthermore, the 2017 observations included inter-site baselines between only five geographic locations for M87, and six locations for Sgr A*, fundamentally limiting the fidelity of image reconstruction on angular scales that resolve the black hole shadow.

The ngEHT concept focuses on overcoming these limits through several key developments. Foremost among these is the deployment of relatively modest-diameter radio dishes at optimized locations to increase baseline coverage. Figure 2 shows that even a 6 m diameter dish in marginal weather conditions can detect long baseline correlated fluxes from Sgr A* and M87 when paired with a large "anchor" aperture. This reflects the fact that the 2017 observations, though using fringe detection algorithms limited to 2 GHz bandwidth, achieved signal-to-noise ratios that were typically in excess of ∼10 and often reached ∼100. In other words, the current EHT is limited by baseline coverage and not sensitivity considerations. Through this increased baseline coverage, the ngEHT will reach image dynamic ranges that exceed 1000:1 for full Earth rotation aperture synthesis observations of M87 and other AGN. Time-lapse movies that capture the dynamics of M87's accretion flow and jet launch by combining bi-weekly observations will achieve similar dynamic ranges (pre-cursor multi-epoch observations are possible with the existing EHT at lower imaging dynamic range). For Sgr A*, which has an Innermost Stable Circular Orbit

(ISCO) period of $\sim\frac{1}{2}$ h, the ngEHT snapshot baseline coverage in 5 min integrations will be sufficient for near real-time video reconstruction. Figure 3 shows the current EHT array and the location of potential new ngEHT sites.
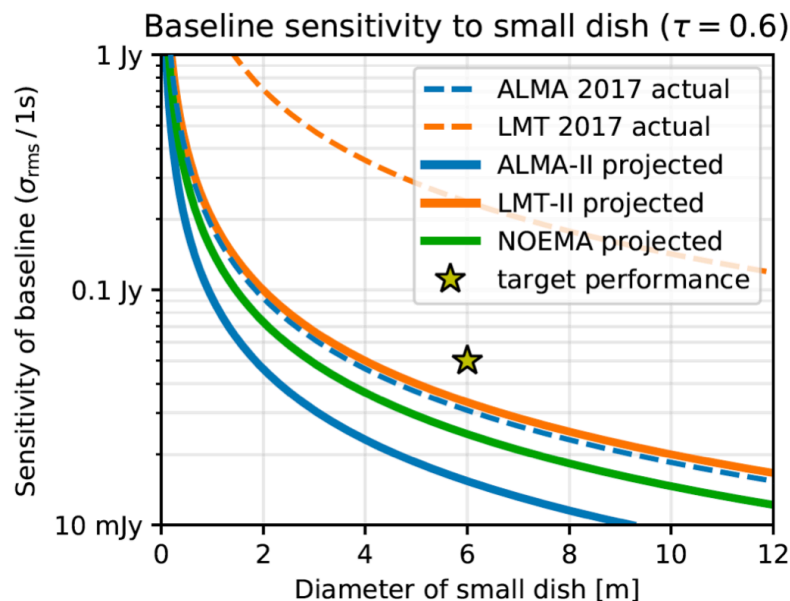
Figure 2. Interferometric baselines between key anchor stations and modest-diameter dishes have sufficient sensitivity to detect target flux densities on time scales of several seconds. A star marks the correlated flux expected for SgrA* and M87 over long ngEHT baselines. Performance for 2017 is taken over 2 GHz of bandwidth and the observed median sensitivity of ALMA and LMT during EHT April 2017 observations. ALMA-II assumes phase referencing using the entire 8 GHz (64 Gbps) of EHT bandwidth, while LMT-II assumes 16 GHz of bandwidth and aperture efficiency of $\eta_A = 0.37$. NOEMA is projected for a 12-element array under nominal weather conditions, and the small ngEHT remote site is evaluated at $\eta_A = 0.5$ and line-of-sight opacity $\tau = 0.6$. Atmospheric phase tracked on rapid timescales at 86 GHz or 230 GHz can be transferred to 345 GHz, allowing for longer coherent integration times and robust measurement at the highest ngEHT observing frequencies.

Figure 3. Current EHT sites (in black), other existing or near-future sites that may join global observations (in red), and potential new ngEHT sites (in blue).

Significant improvements in sensitivity will still be realized through the deployment of wider band receivers and backends, which can now typically digitize 8 GHz per sideband. For a given frequency band, the ngEHT targets dual-sideband and dual-polarization, for a potential Stokes I fringe detection that combines 32 GHz aggregate bandwidth. For any given baseline, this advance results in a net detection threshold that is four times lower than currently achievable.

In addition to this increase in overall received bandwidth, the ngEHT frequency coverage will include the 86 and 345 GHz bands. Routine multi-band operation has several important consequences for ngEHT capability. Each station pair probes distinct spatial frequencies when observing in different bands, and multi-frequency imaging algorithms can make use of the aggregate interferometric coverage to improve image fidelity (e.g., [41]). Observing in the 345 GHz band also improves the angular resolution of the global array by up to 50%. The EHT already offers 345 GHz observing capability on a subset of antennas [42], but not yet simultaneously with 230 GHz. Additional frequency bands also enable analyses and modeling that differentiate between gravitationally lensed achromatic features (e.g., the photon ring) and structures whose appearance have a spectral dependence (e.g., accretion flows and relativistic jets). Through the use of the frequency phase transfer technique (FPT; [43]), VLBI phase solutions determined at lower frequencies can be transferred to higher frequency observations, effectively removing atmospheric phase effects to extend coherent integration times for higher sensitivity. The full case for adding 86 GHz capability that leverages FPT through simultaneous multi-band systems is described in Issaoun et al. [44].

Combined, these enhancements lead to profound increases in array capability. The implementation roadmap for the ngEHT will proceed in two phases with the goal of ultimately adding ∼10 new dishes to the EHT. In Phase 1, a total of six new sites will be developed: four radio dishes will be deployed to new geographic locations (Section 4.4.1); and two existing facilities (the 37 m telescope at MIT Haystack Observatory and a 10 m telescope at the Owens Valley Radio Observatory) will be modified to participate in future observations (see, e.g., [45]). A Phase 2 will add four more telescopes, either by deploying additional new purpose-built telescopes, or by instrumenting planned single dish facilities due to come online by ∼2030 (Section 4.4.2). These phases, when complete, will double the number of dishes in the array recently fielded in the 2022 and 2023 annual EHT observing campaigns (see Section 4.4).

3. Next Generation Science Goals

The ngEHT design has been guided by a series of Key Science Goals (KSGs), developed through a community-driven process of exploration, evaluation, and prioritization. These goals and their associated instrument requirements are presented via a Science Traceability Matrix (STM) in a companion paper [46]; and a series of papers in a Special Issue of *Galaxies*[1] presents science topics in greater detail. Here, we briefly describe several of the ngEHT KSGs, which define the target baseline array architecture, and are summarized in Table 1.

Table 1. Select ngEHT Key Science Goals. For the full Science Traceability Matrix and additional details, see Johnson et al. [46].

Key Science Goal	Source	ngEHT Phase	References
Establish the existence of black hole horizons	M87* Sgr A*	Phase 1 Phase 2	Chael et al. [47]; Dokuchaev and Nazarova [48]
Measure a SMBH's spin	M87* Sgr A*	Phase 2 Phase 2	Palumbo et al. [49] Ricarte et al. [50]
Understanding Black Hole-Galaxy Formation, Growth and Coevolution	AGN Survey	Phase 1	Pesce et al. [51,52]; Ramakrishnan et al. [53]
Reveal how black holes accrete material	M87* Sgr A*	Phase 1 Phase 2	Balbus and Hawley [54]; Yuan and Narayan [55]
Observe localized electron heating and acceleration	M87* Sgr A*	Phase 1 Phase 2	Rowan et al. [56]; Ball et al. [57]
Determine if BH jets are powered by spin energy	M87* Sgr A*	Phase 2 Phase 2	Blandford and Znajek [58]; Tchekhovskoy et al. [59]
Determine jet formation & launching mechanisms	M87* Sgr A*	Phase 1 Phase 2	Blandford et al. [60]
Constraining Properties of the BH Photon Ring	M87* Sgr A*	Phase 2 Phase 2	Johnson et al. [61]; Tiede et al. [62]

3.1. Existence and Properties of Black Hole Horizons

By characterizing the central brightness depression region in black hole images, the ngEHT can directly address the question of the existence of a black hole's horizon. For Magnetically Arrested Disk (MAD) accretion modes, which are favored for M87 [5], emission in the innermost part of the flow originates primarily in the equatorial plane, and the central depression (the "inner shadow") is defined by light paths that cross the event horizon without visiting the emitting region of the accretion system [47,48]. Measuring the shape of this "inner shadow" to be smaller than the photon orbit would correspond to observing the lensed event horizon, allowing estimates of the black hole's mass and spin [47]. For both M87 and Sgr A*, this measurement requires an imaging dynamic range of ~100:1. For Sgr A*, intrinsic variability presents an additional challenge that will require future algorithm development. Furthermore, enhancing the dynamic range of the images with the ngEHT will allow obtaining improved constraints on the brightness ratio between the black hole shadow interior and the observed emission ring. These constraints can be translated to an argument supporting the existence of the event horizon, by putting the most stringent limits on the albedo of the surface of an exotic compact object alternative to a black hole [12], ultimately limited only by the emission and absorption in the foreground by the gas located out of the equatorial plane (e.g., [63]).

3.2. Measurements of the Spin of a SMBH

General relativity predicts that astrophysical black holes are described solely by two properties: their mass and angular momentum (or "spin"). The ngEHT has the opportunity to produce direct secure measurements of a black hole spin through distinctive image features that reflect the imprint of the strongly curved spacetime near the horizon. In particular, images of GRMHD simulations show several robust indicators of spin (for a review, see [50]). The most promising of these is the spiraling polarization pattern around the emission ring [49]. By producing time-averaged polarimetric images of M87 and Sgr A* at both 230 and 345 GHz, the ngEHT will be able to securely measure this pattern and decouple the effects of the spacetime from those of the surrounding plasma (Faraday rotation and conversion), which are steeply chromatic.

3.3. Evolution of Supermassive Black Holes

Though the EHT has to date observed only two SMBHs (M87* and Sgr A*) with horizon-scale angular resolution, numerical simulations of black hole accretion flows (e.g., [5,11]) predict that the "shadow" structure seen toward these sources should be a generic image feature in sufficiently optically thin systems. Measurements of the size of the SMBH shadow can be used to constrain the black hole mass (e.g., [6,10]), and measurements of the near-horizon linear polarization structure may also be able to provide indirect constraints on the black hole spin [49,50,64]. Access to a population of shadow-resolved SMBHs would thus provide an opportunity to make uniquely self-consistent measurements of these spacetime properties, permitting corresponding studies of SMBH formation, growth, and co-evolution with their host galaxies.

The ngEHT is expected to be able to detect up to several dozen SMBHs with sufficient angular resolution and sensitivity to access their masses and spins through measurements of their horizon-scale structure [51,52]. A database of the most promising individual targets is being compiled within the ETHER sample [53].

3.4. Mechanisms of Black Hole Accretion

Despite decades of study, the mechanisms that drive accretion onto SMBHs are still poorly understood (for a review, see [55]). The ngEHT will make the first resolved movies of a black hole accretion flow, allowing a direct study of the dynamics of the turbulent plasma and the role of magnetic fields in providing an effective viscosity that drives infall [54,65].

3.5. Heating and Acceleration of Relativistic Electrons

In low density, low accretion rate systems, such as in M87* and Sgr A*, the Coulomb collision time for both electrons and protons is much larger than the dynamical (accretion) time scale. As a consequence, protons and electrons cannot redistribute their energy and a two-temperature plasma occurs. Assuming that the emission is mainly generated by electrons, their temperature is determined by the interplay between cooling and heating processes [66]. Given, that in low accretion rate systems, the cooling processes can be neglected (cooling time scale larger than the dynamical time scale), the impact of possible electron heating processes on the observed emission from M87* and Sgr A* can be probed.

Two of the main processes for the heating of electrons are turbulent heating (see, e.g., [67,68]) and magnetic reconnection heating (see, e.g., [56]). The results of two-temperature general relativistic magneto-hydrodynamic (GRMHD) simulations showed that magnetic reconnection heating leads to a disk-dominated emission structure while turbulent heating tends to a disk-jet structure [69–72]. The ngEHT with its improved u-v coverage and increased sensitivity will allow us to image and track at the same time the disk and faint jet structures on scales of $100r_g$ ($r_g = GM/c^2$). Together with the multi-frequency capabilities of the ngEHT movies, the total intensity and the spectral evolution can be produced. These movies, in close combination with detailed numerical simulations, can allow us to locate the heating sites and distinguish between the different electron heating processes in M87* and Sgr A*.

3.6. Energy Extraction from Black Holes

Energy from a spinning black hole can be extracted via the Blandford-Znajek (BZ) process [58], an electromagnetic analog of the classic Penrose process [73]. With the ngEHT we will probe this energy extraction mechanism via the generated jet power or more precisely via the so-called BZ-jet power. The BZ-jet power is proportional to the square of the black hole spin and to the square of the magnetic flux crossing the horizon [59]. In addition, the jet power can be measured from the observed spectral energy distribution or from the X-ray luminosity (see [74], for a detailed discussion on jet power estimates).

To compute a theoretical estimate for the BZ-jet power precise measurements of the black hole spin and the magnetic flux are necessary. As mentioned in Section 3.2 of this paper and in Broderick et al. [75], the combined ngEHT observations will provide the black hole spin and black hole mass with sufficient precision. The second quantity in the BZ-jet power, namely the magnetic flux across the horizon can be obtained either via polarimetric ngEHT observations [76] or via the frequency-dependent position of the core, i.e., the core-shift using multi-frequency observations [77]. In both cases the superior detection and imaging capabilities of the ngEHT will allow us to provide answers to this long-standing question of energy extraction from black holes. To perform this measurement for M87, Phase 2 of the ngEHT is required.

3.7. Jet Formation

Based on numerical GRMHD simulations we know that rotating black holes can launch jets via the BZ process (see, e.g., [59,78]). However, once launched the jets need to be accelerated and confined, whereas the associated physical processes behind this acceleration and collimation as well as the jet composition are still being debated (see [60], for a review). The jet composition electron-positron or electron-proton plasma can be probed via circular polarization and a detailed review can be found in the Special Issue by Emami et al. [79].

Details on the fluid structure and the formation process of the jet in M87 can be derived from the velocity field and the jet-to-counter-jet ratio [80,81]. The structure of the velocity field will allow us to probe the stratification of the jet into a fast inner spine and slow outer sheath (see, e.g., [82]). The ngEHT will enable such studies in objects other than M87 by resolving the transversal jet structure, e.g., in Centaurus A [83]. In addition to the poloidal velocity field (spine-sheath structure), the toroidal velocity field plays a crucial

role in determining the formation process of the jet: Is the jet anchored in the accretion disk [84] or is the jet launched from the ergosphere of a rotating black hole [58]. Extracting the velocity field of the jet requires multi-frequency observations and a high cadence of observations. To avoid the "contamination" of the velocity field by secondary effects, i.e., by Kelvin-Helmholtz instabilities or re-collimation shocks (triggered by changes in the ambient medium) scales up to $100r_g$ are sufficient. In order to determine the velocity field in M87 the ngEHT in Phase 1 is required.

3.8. Constraining Properties of the Black Hole Photon Ring

One of the clearest predictions motivated by the first black hole images is that the observed ring of emission should exhibit a fine sub-structure: nested concentric rings, each formed by light rays that make successively more orbits around the photon shell region, located very close to the black hole's event horizon [61]. Each sub-ring is a lensed image of the surrounding accretion and jet emission with inner sub-rings becoming exponentially fainter and narrower. The structure of the primary ($n = 0$) ring, observed by the EHT, depends on a combination of the local spacetime and the detailed emission structure on Schwarzschild radius scales, while subsequent sub-rings ($n \geq 1$) asymptotically approach the true photon orbit, which is dependent exclusively on the spacetime metric [13]. Detection of the $n = 1$ ring, formed by photons that make a half-orbit around the black hole, would be important confirmation of this untested prediction of General Relativity and lead to new tests of GR in highly curved space–time [75,85]. Robust extraction of this feature with the ngEHT will require the longest Earth baselines at 345 GHz and geometric model fitting that uses multiple frequencies [62]. This science goal would be a target of the fully realized (Phase 2) ngEHT.

4. Optimizing the ngEHT Reference Array

The scientific performance of an array generically benefits from the addition of new stations, regardless of where those stations are located. However, when constrained by a fixed budget or a fixed number of new dishes to be added, determining the optimal placement of the new dishes is a challenge that requires finding a balance between many—often conflicting—objectives. For instance, science goals that require high angular resolution favor array configurations with many long baselines, while goals that involve high-fidelity imaging on large fields of view instead favor configurations containing dense short-baseline coverage. Similarly, while atmospheric opacity considerations favor the highest and driest locations, such sites are often remote and lack critical infrastructure, significantly driving up construction and operating costs. Any array configuration that one ultimately arrives at necessarily hinges on a non-unique choice about what exactly constitutes "optimality", and the result can depend sensitively on how one weighs the many relevant considerations when doing so.

In this section, we detail some of the considerations that are entering into the design process for the ngEHT array configuration. Section 4.1 describes how we have selected an initial pool of candidate sites to consider, Section 4.2 describes our procedure for simulating realistic ngEHT observations, and Section 4.3 details several metrics that we use to evaluate array quality. Section 4.4 describes our evaluation of the many different candidate arrays and discusses a strategy for translating array performance into site selection. Various details relevant to the site selection procedure are provided in Appendix A.

4.1. Candidate Sites

From most locations on the surface of the Earth, atmospheric opacity prevents observations at the primary ngEHT frequencies of 230 GHz and 345 GHz. We thus take our starting pool of candidate sites from [86], who identified sites with favorable atmospheric transmission properties for 230 GHz and 345 GHz observations during the March/April typical EHT observing season; the candidate sites are shown in Figure 3 and listed in Table A1.

Given the selection on atmospheric opacity performed in [86], the candidate sites are naturally situated in the highest and driest locations. Figure 4 shows the highest-elevation locations around the globe, and Figure 5 shows where the mean level of precipitable water vapor (PWV) is lowest throughout the year. We have computed the PWV using atmospheric data from the MERRA-2 database [87]. The PWV at a particular location is determined by integrating the water vapor through the column of atmosphere above that location (see, e.g., [88]),

$$\text{PWV} = \frac{1}{\rho g} \int_0^{P_{\text{surf}}} \frac{q(P)}{1 - q(P)} dP. \tag{1}$$

Here, $q(P)$ is the specific humidity, P is the atmospheric pressure, P_{surf} is the atmospheric pressure at the surface, $\rho \approx 1\,\text{g cm}^{-3}$ is the mass density of water, and $g \approx 9.81\,\text{m s}^{-2}$ is the acceleration of gravity at the surface of the Earth. MERRA-2 provides both P and q in 42 different atmospheric layers as a function of geographic location and time.
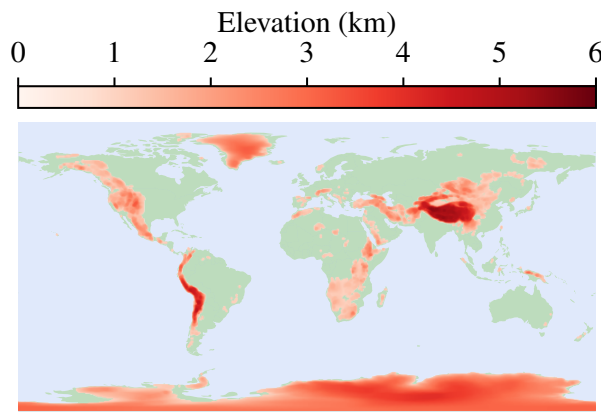
Figure 4. Global elevation map. Locations with elevations above 1000 m are shaded red, with darker colors indicating higher elevations.

4.2. Synthetic Data Generation

We evaluate candidate array performance using synthetic observations of the key science targets M87* and Sgr A*. For source models, we use the results of general relativistic magnetohydrodynamic (GRMHD) simulations that have been post-processed using ray-tracing and radiative transfer codes to produce images at the 230 GHz and 345 GHz observing frequencies appropriate for the ngEHT. Our M87* source model comes from the simulations carried out in [71], and our Sgr A* source model comes from the simulation library produced in [11].

We generate synthetic datasets using the `ngehtsim`[2] library. Given a candidate ngEHT array configuration and a source model, `ngehtsim` uses `eht-imaging` [89,90] to sample the Fourier transform of the source at the (u, v)-coverage corresponding to the array. Thermal noise σ_{ij} on a baseline between stations i and j is determined by the radiometer equation,

$$\sigma_{ij} = \frac{1}{\eta_q} \sqrt{\frac{\text{SEFD}_i \text{SEFD}_j}{2 \Delta \nu \Delta t}}, \tag{2}$$

where $\Delta \nu$ is the observing bandwidth, Δt is the integration time, SEFD is the station system equivalent flux density, and $\eta_q = 0.88$ is an efficiency factor associated with 2-bit quantization during data collection [91]. We determine SEFDs for each station as a function of time using

$$\text{SEFD} = \frac{2k T_{\text{sys}}}{A_{\text{eff}}} e^\tau, \tag{3}$$

where k is the Boltzmann constant, τ is the (time-dependent) line-of-sight atmospheric opacity, A_{eff} is the effective collecting area of the telescope,

$$T_{\mathrm{sys}} = T_{\mathrm{rx}} + T_{\mathrm{atm}}\left(1 - e^{-\tau}\right) \tag{4}$$

is the system temperature, T_{rx} is the receiver temperature, and T_{atm} is the temperature of the atmosphere. We determine T_{atm} using historical atmospheric data from the MERRA-2 database [87], and τ is obtained by passing the atmospheric state information from MERRA-2 through the *am* radiative transfer code [92].
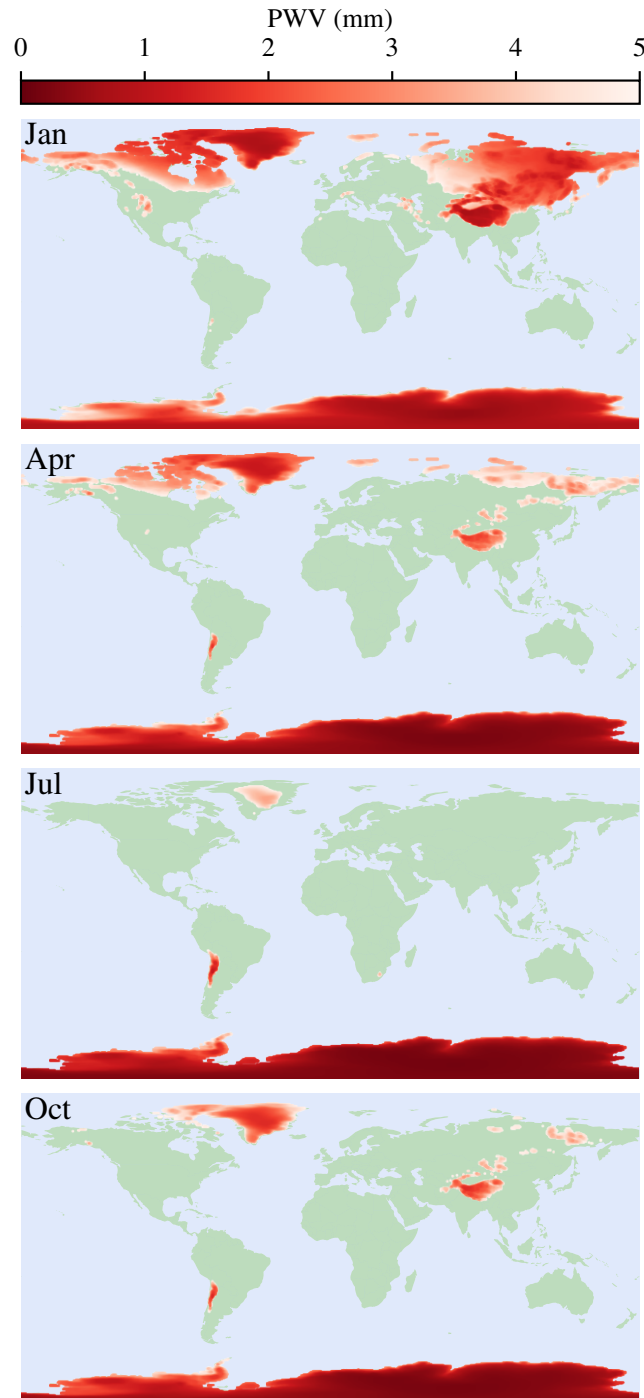
Figure 5. Locations around the globe with mean PWV less than 5 mm, in January (**top**), April (**second from top**), July (**second from bottom**), and October (**bottom**). A darker red coloring indicates a lower value of mean PWV, and only locations with elevations above 50 m are colored. We have determined the PWV via Equation (1) using atmospheric data from MERRA-2 [87], and the average is taken over all available data between 2012 and 2022.

For the synthetic datasets in this section, we use a Stokes I bandwidth of $\Delta\nu = 16\,\text{GHz}$ (for ngEHT) or $\Delta\nu = 2\,\text{GHz}$ (for EHT) at each of two frequency bands, one centered at 230 GHz and the other centered at 345 GHz. We use an integration time of $\Delta t = 10\,\text{min}$, which is assumed to be enabled by suitable phase calibration, with a 50% duty cycle (i.e., 10 min on-source followed by 10 min off-source); the total duration of each observation is 24 h. We assume receiver temperatures T_{rx} of 50 K at 230 GHz and 75 K at 345 GHz.

We emulate fringe-finding by applying a signal-to-noise ratio (SNR) thresholding scheme to the generated visibilities. The scheme employs a variant of the "fringe groups" strategy from Blackburn et al. [93] for assigning reliable measurements from a set of baseline visibilities: if visibility does not achieve an equivalent SNR of 5 (phase error of 11.5 degrees) on an integration time of 10 s (at 230 GHz) or 5 s (at 345 GHz), and if the stations comprising the baseline associated with that visibility do not participate in other baselines that achieve the requisite SNR, then that visibility is considered to be not measured and it is flagged from the dataset. Note that for the stations with dual-frequency capabilities, both of the frequency bands are checked simultaneously; if either one of the two frequency bands has an SNR that satisfies the threshold condition, then we assume that both bands can be detected. This multi-frequency fringe groups scheme emulates frequency phase transfer across the bands (see, e.g., [94]). We only emulate FPT when simulating ngEHT data; when simulating EHT data, we apply only the single-frequency fringe groups scheme.

4.3. Array Performance Metrics

The analysis methods utilized by the EHT for performing measurements of physical interest using VLBI data are in general highly computationally expensive to evaluate. Further, the added value of a particular set of new sites is non-linear in the number of sites; the number of new baselines is quadratic in the number of existing sites, and the value of an individual site is sensitive to its position with respect to existing dishes.

To evaluate the performance of candidate ngEHT array configurations without running computationally expensive analysis pipelines (such as imaging or model-fitting), we utilize metrics of array performance that are based on pre-analysis quantities. We primarily employ two metrics: one metric that quantifies the (u, v)-coverage and another metric that quantifies the aggregate baseline sensitivity. We compute the array performance metrics using synthetic observations at frequencies of 230 GHz and 345 GHz, which drive the key science goals of the ngEHT. While 86 GHz is an important addition that enables improved detection prospects at the higher frequencies (see Section 7.1), it serves primarily a calibration-related role and thus is not included in our (u, v)-coverage or baseline sensitivity metric computations. We note, though, that ngEHT sites could potentially be included in 3 mm wavelength VLBI networks (e.g., GMVA) or as part of ngVLA observations [44].

We use as our quantification of (u, v)-coverage quality the (u, v)-filling fraction metric (FF metric), defined in Palumbo et al. [95] as the fraction μ_{ff} of the area enclosed by a bounding circle in (u, v) of radius $1/\theta_{\text{res}}$ that is covered by the two-dimensional convolution of the coverage with a circular disk of radius $1/\theta_{\text{FOV}}$. Here, θ_{res} and θ_{FOV} are array performance specifications based on imaging expectations, and they are not predicted directly by the coverage; Figure 6 provides an illustration of how the FF metric is calculated. Palumbo et al. [95] found that as the filling fraction increases, imaging performance in compact imaging examples improves steadily until it flattens to a constant factor of the diffraction-limited image fidelity near $\mu_{\text{ff}} \gtrsim 0.5$. The FF metric naturally demands greater coverage for equivalent μ_{ff} as expectations of the imaging field of view θ_{FOV} increases; however, μ_{ff} does not capture the relative information density of the Fourier plane, and for many source morphologies, the importance of Fourier coverage decreases with radius from the (u, v)-coordinate origin. In this paper, we assume $\theta_{\text{res}} = 14\,\mu\text{as}$ (i.e., the angular resolution of an Earth-diameter baseline observing at 345 GHz) unless otherwise specified, but we use several different fields of view; when quoting FF metric values, we will thus specify the corresponding assumed field of view using the notation $\mu_{\text{ff}}(\theta_{\text{FOV}})$.
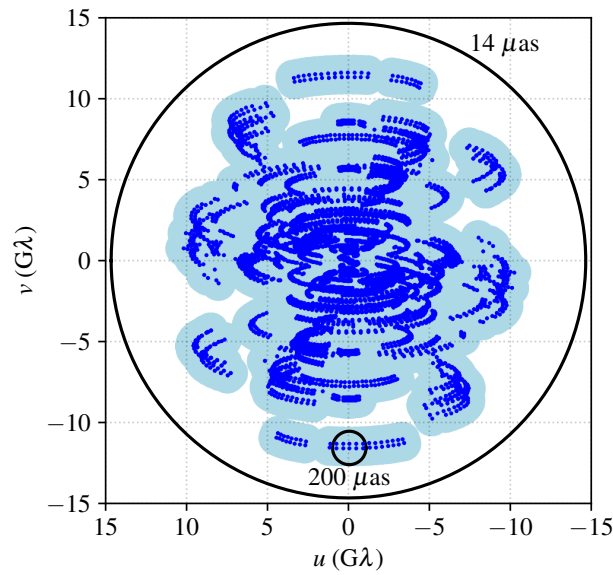
Figure 6. Illustration of the (u, v)-filling fraction metric described in Section 4.3 (see also Palumbo et al. [95]). Given some (u, v)-coverage—shown here by the blue points for a mock observation of M87 using the full ngEHT Phase 1 array in April—the FF metric is a measure of how much area within a circular region of radius $1/\theta_{\mathrm{res}}$ is sampled, after convolving the coverage with a disk of radius $1/\theta_{\mathrm{FOV}}$. In this case, $\theta_{\mathrm{res}} = 14\,\mu\mathrm{as}$ and $\theta_{\mathrm{FOV}} = 200\,\mu\mathrm{as}$. The convolved coverage is shaded in light blue, and takes up a fraction $\mu_{\mathrm{ff}} = 0.5$ of the area of the outer circle.

For our quantification of aggregate array sensitivity, we use the point source sensitivity (PSS) metric,

$$\mathrm{PSS} = \left(\sum_{i=1}^{N} \frac{1}{\sigma_i^2} \right)^{-1/2}, \tag{5}$$

where σ_i is the value of the thermal noise on visibility i (see Equation (2)), and the sum is taken over all visibilities in the dataset. The PSS metric, which has units of flux density, quantifies the sensitivity that the array could in principle achieve when measuring the flux density of a point source. It naturally folds in not only the observing bandwidth and diameter of each telescope in the array, but also the amount of mutual visibility that each site has with every other as well as the atmospheric transmission at each site.

4.4. Site Selection

The stringent atmospheric opacity requirements for observing at millimeter wavelengths means that only a small number of locations around the globe are suitable candidates (see Section 4.1). Given that the list of candidate sites presents a finite number of discrete locations on the globe where telescopes could be placed, we could in principle evaluate all possible new array configurations. The ability to confine the site search space to a finite number of options in this way is fairly unique to high-frequency VLBI, and it informs our optimization strategies below; the analogous site selection problem for connected-element arrays (e.g., VLA, ALMA, ngVLA) and low-frequency VLBI arrays (e.g., VLBA, SKA) presents a qualitatively different challenge.

In practice, though the number of possible new array configurations is finite, the space remains large and difficult to search comprehensively; the number of possible new array configurations that could be made using the 44 sites listed in Table A1 is approximately 1.8×10^{13}. Additionally, we would like to ensure that the selected sites enable the ngEHT array to perform well across all of the following situations:

- in observations of both M87* and Sgr A*;
- during observations that take place throughout the year;

- when observing alongside any subset of the EHT.

The performance of each candidate array must also be evaluated using several different quality metrics (see Section 4.3) that correspond to the various scientific goals. All of the above considerations result in multiplicative factors that further increase the expense of a comprehensive analysis.

Given the difficulty of comprehensively searching all possible combinations of new stations, we instead partition our site selection efforts into two stages corresponding to the two anticipated phases of ngEHT development. In the first stage—corresponding to ngEHT Phase 1—we consider the selection of three new sites from the pool of candidates. The availability of three 6.1-m BIMA dishes for refurbishment and relocation (see Section 7.5) provides a pathway to realizing a Phase 1 ngEHT array on a shorter (∼few-year) timescale than it will take to field a larger array of newly constructed dishes. Optimizing for only three new sites at a time also reduces the number of site combinations to only $\binom{44}{3}$ = 13,244. In the second stage of the site selection analysis—corresponding to ngEHT Phase 2—we then consider the selection of five new sites from the remaining pool of candidates, corresponding to $\binom{41}{5}$ = 749,398 different site combinations. Dividing the optimization strategy into two stages in this way, and selecting a specific target number of new sites in each stage, substantially reduces the computational cost of optimizing the array configuration.

The sites and frequency configurations corresponding to the selected Phase 1 and Phase 2 ngEHT arrays are listed in Table 2.

Table 2. Site participation and frequency capabilities for the EHT and both phases of the ngEHT array. For the first column, EHT sites with existing 86 GHz capability are noted, but the EHT does not currently support 86 GHz operation; and some of these 86 GHz receivers cannot be used simultaneously with higher frequency receivers. In each of the three rightmost columns, sites that do not participate in the specified array are indicated with a "-" sign. Multi-frequency capabilities are indicated with a "+" sign; e.g., "230 + 345" indicates that the station can observe at both 230 GHz and 345 GHz simultaneously, whereas "230 345" indicates that it can only observe at each frequency separately. For completeness, we list in the rightmost column an alternative incarnation of the ngEHT Phase 2 array, in which we forgo the need to field new telescopes by relying instead on external facilities that are anticipated to come online in the next few years (see Section 4.4.3). For this alternate case, the JELM site would be added in Phase 1. [†] This site is being developed independently of the ngEHT.

Site	Status	EHT			ngEHT Phase 1			ngEHT Phase 2			ngEHT Phase 2 (alt.)		
ALMA	existing	86	230	345	86	230	345	86	230	345	86	230	345
AMT	planned [†]		-			-			-		86 + 230 + 345		
APEX	existing		230	345	86	230	345	86	230	345	86	230	345
BOL	planned		-			-		86 + 230 + 345				-	
CNI	planned		-		86 + 230 + 345			86 + 230 + 345			86 + 230 + 345		
GLT	existing	86	230	345	86 + 230 + 345			86 + 230 + 345			86 + 230 + 345		
HAY	existing		-		86 + 230			86 + 230			86 + 230		
IRAM	existing	86 + 230		345	86 + 230		345	86 + 230		345	86 + 230		345
JCMT	existing	86	230	345	86 + 230 + 345			86 + 230 + 345			86 + 230 + 345		
JELM	planned		-			-		86 + 230 + 345			86 + 230 + 345		
KILI	planned		-			-		86 + 230 + 345				-	
KP	existing	86	230		86 + 230			86 + 230			86 + 230		
KVNPC	planned [†]		-			-			-		86 + 230 + 345		
KVNYS	existing		-			-			-		86 + 230 + 345		
LCO	planned		-		86 + 230 + 345			86 + 230 + 345			86 + 230 + 345		
LLA	planned [†]		-			-			-		86 + 230 + 345		
LMT	existing	86	230		86 + 230 + 345			86 + 230 + 345			86 + 230 + 345		
NOEMA	existing	86	230	345	86 + 230		345	86 + 230		345	86 + 230		345
OVRO	existing		-		86 + 230			86 + 230			86 + 230		

Table 2. *Cont.*

Site	Status	EHT		ngEHT Phase 1	ngEHT Phase 2	ngEHT Phase 2 (alt.)
SGO	planned	-		-	86 + 230 + 345	-
SMA	existing	230	345	230 345	230 345	230 345
SMT	existing	230	345	86 + 230 + 345	86 + 230 + 345	86 + 230 + 345
SPM	planned	-		86 + 230 + 345	86 + 230 + 345	86 + 230 + 345
SPT	existing	230		86 + 230 + 345	86 + 230 + 345	86 + 230 + 345
SPX	planned	-		-	86 + 230 + 345	-

4.4.1. Phase 1

To determine the optimal locations for the three new 6.1 m Phase 1 dishes, we carry out a survey of all possible three-station combinations of the 44 sites listed in Table A1. For each candidate set of three sites, we explore the performance of the resulting array (1) for observations of both M87* and Sgr A*, (2) under weather conditions appropriate for January, April, July, and October, and (3) when observing alongside four different variants of the existing EHT array (specified in the top section of Table A2). These pre-existing array variants include various subsets of the EHT array, as well as the HAY and OVRO dishes that are expected to be outfitted with ngEHT equipment (see Section 2). We evaluate each candidate array using the metrics described in Section 4.3 for 100 instantiations of the weather conditions at each site, from which we then take median values to establish typical performance.

After evaluating all candidate arrays, we determine a "performance score" for each array according to its average ranking across the full suite of observing parameters, e.g., if a particular array is ranked first for one set of observing parameters, ranked third for a second set of observing parameters, and ranked fifth for a third set of observing parameters, then its performance score would be $(1 + 3 + 5)/3 = 3$. Arrays with smaller values of the performance score are those that have performed well across a range of observing parameters. Figure 7 shows the top 1% of all three-station candidate site combinations after ranking them by their performance scores, with each set of sites plotted as a connected three-baseline triangle. We identify six heavily populated clusters of high-performing site combinations:

- An "eastern cluster" containing two sites in South America and either CNI or, less frequently, one of the other mainland European sites (BGA, SKS, SPX).
- A "western cluster" containing two sites in South America and a site in North America, most typically either SPM, PIKE, or FAIR.
- A "northern cluster" containing two sites in South America and GLTS, or less commonly with BGK.
- A "southern cluster" containing two sites in South America and one of the Antarctic Dome sites.
- An "equatorial cluster" containing one site in South America, one site in North America, and CNI.
- A "polar cluster" containing one site in South America, GLTS, and one of the Antarctic Dome sites.

We see that the most favored sites tend to be those that are able to leverage simultaneous observability with existing sites. The overrepresentation of existing sites in the Western hemisphere means that sites in the Eastern hemisphere—particularly those in Asia and New Zealand—are correspondingly penalized.

To select from among the top-performing three-site combinations, we impose additional, more qualitative considerations. We disfavor the northern, southern, and polar clusters because they contain sites that are unable to observe either M87* (in the case of the Antarctic sites) or Sgr A* (in the case of GLTS and BGK). The Eastern and Western clusters suffer from a similar asymmetry, in that they include sites that have little mutual visibility

with existing American and European stations, respectively. The equatorial cluster provides the most balance in terms of site geography, and it contains the three most favored regions for a new site: South America, North America, and CNI. Several of the South American sites are comparably well-represented among the top site combination candidates, as are a couple of the North American sites. After additionally accounting for initial site cost estimates and favoring lower-cost sites, we settle on the three-site combination of CNI, LCO, and SPM as our fiducial ngEHT Phase 1 additions.
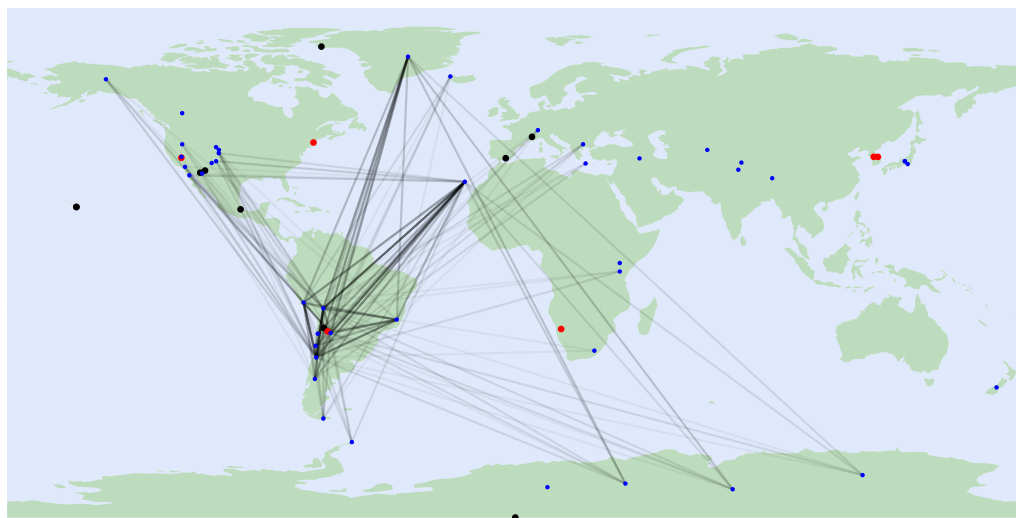
Figure 7. Top performing 1% of all three-station candidate site combinations from the Phase 1 exploration (see Section 4.4). Dots follow the same color convention as in Figure 3: black are current EHT sites, red are existing or near-future sites that may join global observations, and blue are potential new ngEHT sites. Three-station candidate site combinations are shown as connected black triangles.

4.4.2. Phase 2

In the second stage of our site selection analysis—corresponding to ngEHT Phase 2— we consider the addition of five new 9 m sites to the previous three 6.1 m sites determined from the Phase 1 selection. We explore the same observing targets and weather conditions as for the Phase 1 exploration, but we use updated pre-existing arrays that include the Phase 1 sites (see the bottom section of Table A2). We again evaluate each candidate array using the metrics described in Section 4.3 for 100 instantiations of the weather conditions at each site, and we use median metric values to establish typical performance.

The selection process for Phase 2 is ongoing, but preliminary results indicate that the combination of BOL, JELM, KILI, SGO, and SPX would provide a strong improvement to the array coverage. We thus take these sites to be our fiducial ngEHT Phase 2 additions for the purposes of this paper.

4.4.3. Alternate Staging of New Sites

Several new radio telescopes that could be used for ngEHT observations are planned to become operational in the coming years. Thus, an alternative staging approach would be to augment Phase 1 by adding JELM to the three new sites described in Section 4.4.1, and Phase 2 could then consist solely of the following planned telescopes: the LLAMA telescope in Argentina, the AMT in Namibia, the KVNYS telescope near Seoul, Korea, and the KVNPC telescope (currently under construction) near Pyeongchang, Korea. Together, the four Phase 1 sites (CNI, JELM, LCO, SPM) combined with OVRO, HAY, and the four planned telescopes (LLAMA, AMT, KVNYS, KVNPC) would constitute a near-doubling of the existing EHT array and would achieve comparable (u, v)-coverage to that provided by the array described in Section 4.4.2. This alternate pathway to a Phase 2 ngEHT would also provide capabilities sufficient to achieve all ngEHT Key Science Goals.

4.4.4. Baseline Coverage

Simulated EHT coverage for the array fielded during the 2023 observing campaign is shown in Figure 8. The enhanced baseline coverage that will be provided by the ngEHT Phases 1 and 2 is shown in Figures 9 and 10. In Figure 9, the JELM station has been added to reflect a Phase 1 array as described in Section 4.4.3, while Figure 10 shows the array as described in Section 4.4.2. Snapshot coverage for Sgr A* observations is shown in Figure 11, indicating that 1-min integrations produce spatial frequency sampling that can be used for increasingly detailed dynamical modeling.
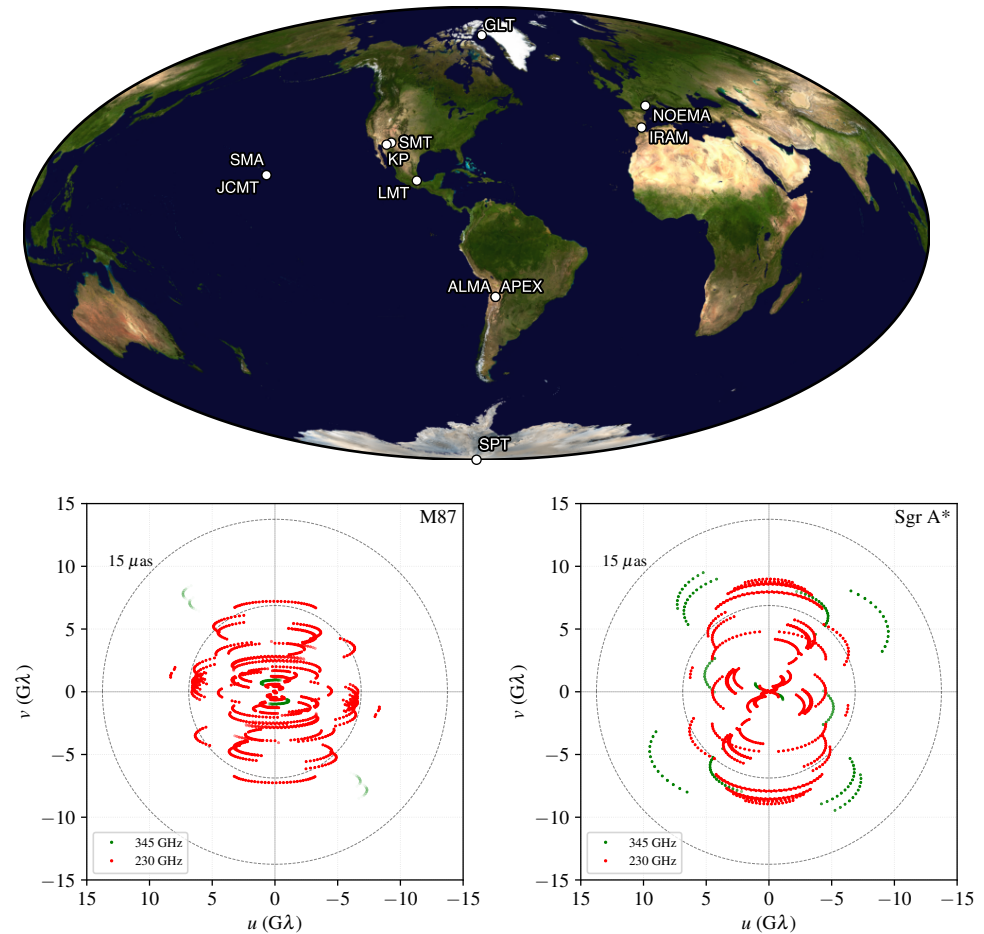
Figure 8. (**Top**) Current EHT array (2023). (**Bottom**) Interferometric coverage for M87* and Sgr A* at 230 & 345 GHz, assuming April observing conditions and a minimum observable elevation of 10 degrees. The coverage reflects estimated detections made through simulating M87* and Sgr A* models at both frequencies with the EHT array as fielded in 2023 (see Table 2, and Section 4.2). Note that for the EHT in 2023, 230 GHz and 345 GHz observations cannot be made simultaneously, so the coverage shown cannot be combined to form a full image (as is possible in the ngEHT Phase 1 and Phase 2 arrays). The opacity of each plotted data point is proportional to how frequently it is expected to be detected. The outer and inner dashed circles mark baseline lengths corresponding to angular scales of 15 μas and 30 μas, respectively.
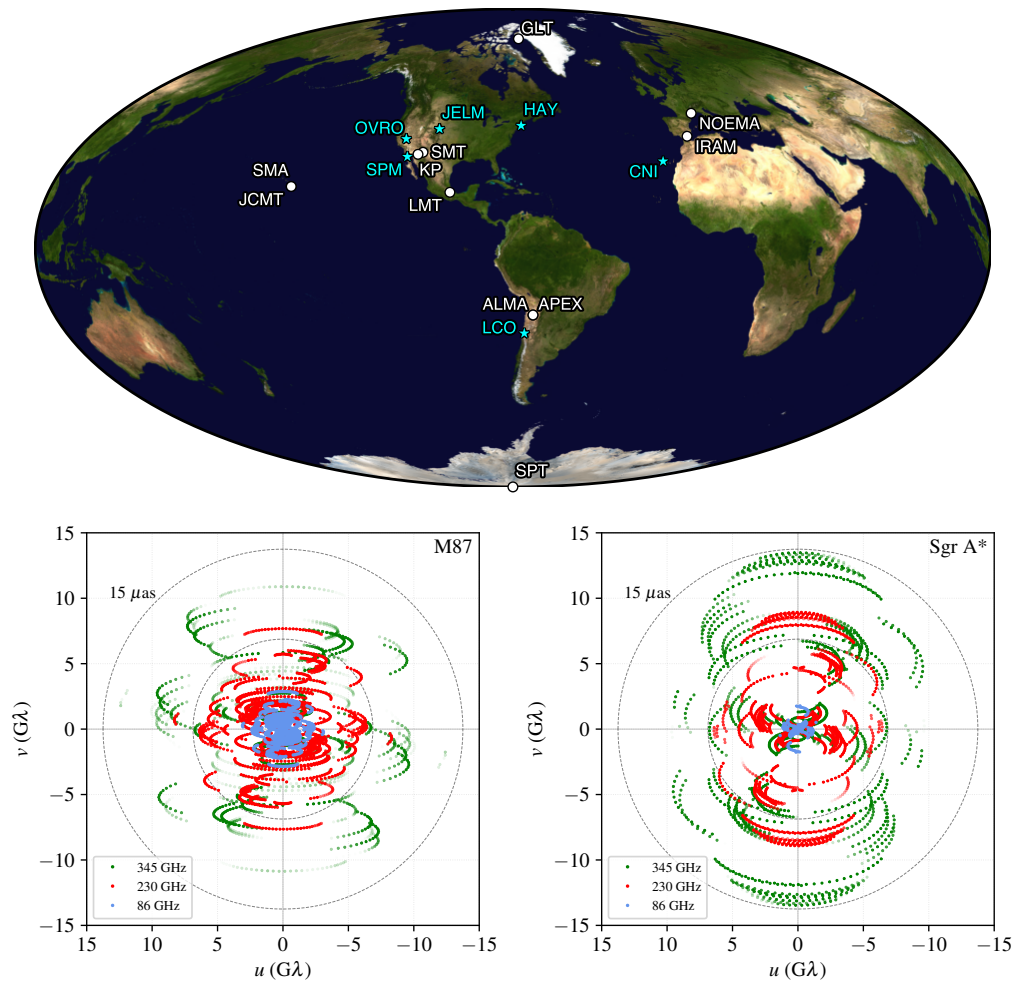
Figure 9. (**Top**) ngEHT Phase 1 array; white sites are current EHT dishes, blue sites are ngEHT sites. (**Bottom**) Interferometric coverage for M87* and Sgr A* at 86 GHz, 230 GHz, and 345 GHz, assuming April observing conditions and a minimum observable elevation of 10 degrees. The coverage reflects estimated detections made through simulating M87* and Sgr A* models at all three frequencies with the ngEHT Phase 1 array (see Table 2 and Section 4.2). Sites without multi-frequency capabilities are assumed to be observed only at their highest frequency. The opacity of each plotted data point is proportional to how frequently it is expected to be detected. The outer and inner dashed circles mark baseline lengths corresponding to angular scales of 15 μas and 30 μas, respectively.
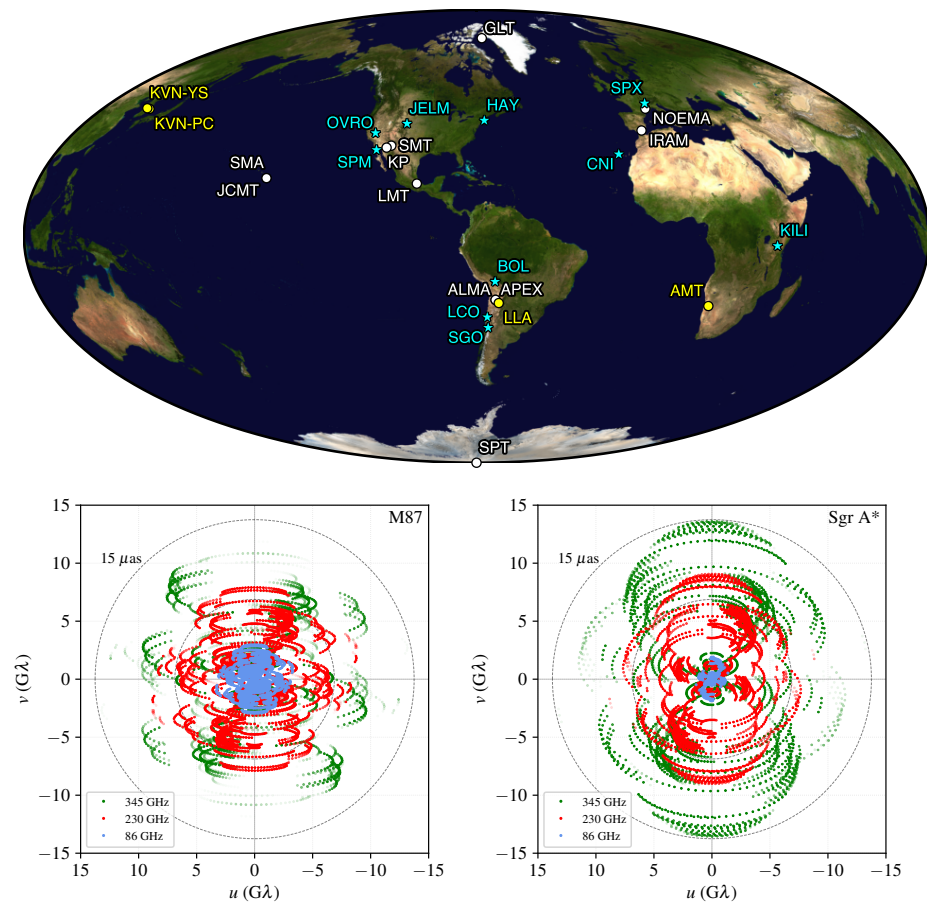
Figure 10. (**Top**) ngEHT Phase 2 array; white sites are current EHT dishes, blue sites are ngEHT sites, and yellow sites are planned or existing facilities that may join (ng)EHT observations and a minimum observable elevation of 10 degrees. (**Bottom**) Interferometric coverage for M87* and Sgr A* at 86 GHz, 230 GHz, and 345 GHz, assuming April observing conditions. The coverage reflects estimated detections made through simulating M87* and Sgr A* models at all three frequencies with the ngEHT Phase 2 array (see Table 2 and Section 4.2). Sites without multi-frequency capabilities are assumed to be observed only at their highest frequency. The opacity of each plotted data point is proportional to how frequently it is expected to be detected. The outer and inner dashed circles mark baseline lengths corresponding to angular scales of 15 µas and 30 µas, respectively.
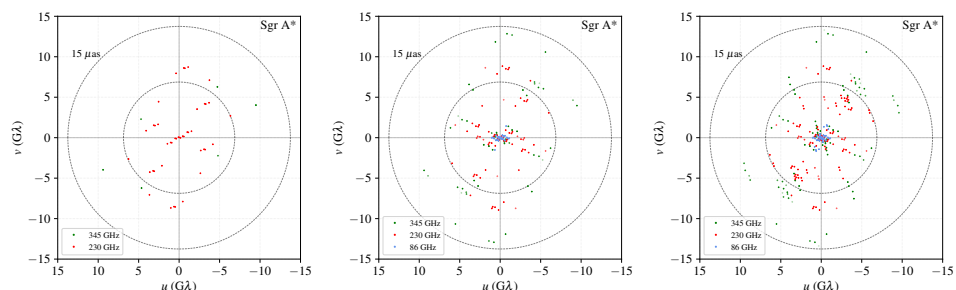
Figure 11. Representative snapshot coverage of SgrA*. For the EHT in 2023 (**left**), ngEHT Phase 1 (**middle**), and ngEHT Phase 2 (**right**), snapshot coverage for 1-min integrations on SgrA* is shown. The increase in spatial frequency sampling enables dynamic modeling of SgrA* with time resolution that is well matched to the dynamical time scales of the source. The outer and inner dashed circles mark baseline lengths corresponding to angular scales of 15 µas and 30 µas, respectively.

5. Operating Modes

Key Science Goals (KSGs) motivate five basic operation modes of the ngEHT, which enable specific science use cases. Details and constraints of each mode are defined by cost/benefit analyses and feasibility studies. Factors to be considered in this analysis include time allocation at various sites, weather, data throughput with implications for disk inventory and correlation, reliability and up-time, and maintenance strategy. The following five subsections provide a narrative summary for each of the five envisaged operating modes of the ngEHT, which are then summarized with salient characteristics in Table 3.

Table 3. The five ngEHT operating modes and selected salient characteristics of each.

OpsMode	Stations in Array	Cadence & Duration	Science Case
Campaign	14 to 21	once per year 7-day session	Sgr A*, M87 blazars, jets
Long term monitoring	5 to 20	once per 3 to 5 days, for 3 to 7 months	M87* & blazar kinematics, Sgr A* flares
Target of Opportunity	3 to 6	once per week during obs. season	flares, gravitational waves
CMF	14 to 21	during Campaign	AGNs, black hole binaries
Beyond ngEHT	1 to 10	dependent on science case	stellar birth, fast radio bursts

5.1. Campaign

This is a single epoch annual multi-day campaign, which is an extension of the standard annual campaign already executed by the Event Horizon Telescope (EHT). The 11 EHT sites defined by those used in the 2022 EHT array are assumed to participate with the ngEHT sites. In this mode, dedicated tracks are based on clearly defined, community-prioritized science cases, in some cases led by a principal investigator.

The campaign mode pursues M87 and Sgr A* science cases with enhanced capability relative to EHT due to improved sensitivity and great UV coverage from the larger 21 site array. This results in enhanced M87 imaging, snapshot sensitivity for Sgr A* movies, and studies of blazar jet collimation.

5.2. Long-Term Monitoring

The long-term monitoring mode uses extended duration and more frequent cadence observations with a smaller subset of the existing EHT sites participating. The ngEHT sites enable this mode through their purpose-designed flexibility and dedicated time allocation for VLBI.

Several multi-week observations over the course of the year once again have dedicated tracks based on clearly defined, community-prioritized science cases. These science cases are in the broad areas of M87* movies, blazar kinematic studies, and Sgr A* flaring activity monitoring. As an example, to continuously track changes in the M87* appearance (M87* movies), reconstructing images separated by the expected coherence timescale ($\sim$50 GM/c^3 $\approx$ 20 days) is needed. A single-year EHT campaign may only last about a week [1]—too short for a significant change in the source appearance, while combining results from separate years only provides uncorrelated source snapshots, without the ability to track continuous motion of the flow features [96]. Similarly, in the published EHT analyses of blazar observations [97–99] short duration of the EHT campaigns, and the lack of repeated observations on timescales of weeks or months, has been recognized as the main factor limiting the current EHT ability to study jet kinematics.

5.3. Target of Opportunity

Target of Opportunity (ToO) is an agile operational follow-up by ngEHT to an unpredictable event observed with another facility. It involves ad hoc subarrays of the 11 existing EHT sites—those that are available—while all of the ngEHT dedicated sites will be made available for suitably scientifically interesting ToO observations. Broad science areas are expected to be in the area of flares, gravitational waves, and fast radio burst counterparts.

5.4. Coordinated Multi-Facility

The Coordinated Multi-Facility (CMF) mode is characterized by coordinated, multi-facility, multi-messenger observations involving multiple ngEHT sites and at least one other ground or space instrument (e.g., Chandra, the GRAVITY instrument, and any of various optical/IR facilities). This CMF mode is a planned continuation of the successful EHT Multi-Wavelength campaigns (see [100]).

The broad science areas are expected to be multi-wavelength studies of Active Galactic Nuclei, binary and singular black holes.

5.5. Beyond ngEHT

This single-dish mode covers any observation that is performed outside the core ngEHT science mission, but will still be part of the ngEHT operating model due to local institutional requirements or synergies with other communities or facilities.

Science is expected to be in the broad area of star-forming regions, fast radio bursts, and astronomical maser studies of transitions in the ngEHT RF bands.

6. Data Processing

The next-generation (ngEHT) expands upon the existing 11-station EHT with around 10 additional small-dish antennas as well as simultaneous 230/345 GHz observations. In addition to the roughly ~10-fold increase in aggregate data rate across the entire array, the ngEHT is expected to operate as a full-season agile observatory as opposed to the ~few observing days per year of the current EHT. When all participating sites are observing, one night of ngEHT produces around ~10 PB of raw data (around 0.5 PB per site), resulting in up to a ~couple hundred PBs per year that must be processed. An efficient streamlined approach to data processing and management is required to facilitate media turn-over and to deliver quality assured science-ready data products in a timely manner.

The large data rates and volumes of the ngEHT motivate continued adoption and assimilation of new technologies, which has allowed a rough tracking of Moore's law over two decades of global mm-VLBI development (Figure 1). On the timescale of a ~decade, we anticipate a transition from Hard Disk Drives (HDDs) to Solid State Disks (SSDs) for recording and eventually transport, which provides high-bandwidth, high-density, and power-efficient I/O. SSDs carry a gradually narrowing cost premium of 5–10 times that of HDDs (in $/TB), but use of SSDs would allow ngEHT recording systems to keep up with the ngEHT data rates while staying within practical power, weight, and space footprints for efficient media handling, staging, and transport.

GPU's have become the platform of choice for massively parallel vector/tensor calculations due to their efficiency and ease of use, and they are being researched or already adopted for efficient VLBI correlation across several experiments. The "embarrassingly parallel" nature of VLBI correlation is suitable for high-throughput computing (HTC) workflows, and the irregular scheduling of VLBI observations means that on-demand scalable computational resources are desirable.

6.1. Data Transport

While observing, the ngEHT will produce an aggregate ~5 Tbps of digital signal data that must ultimately be transported from remote sites to a central location for processing. Similar to the EHT, the only currently available means for moving such a large total volume of data from the (sometimes very-) remote locations in a reasonable amount of time is

by physical transport of recorded media. Some VLBI arrays, such as the European VLBI Network[3] (EVN) are able to transport data electronically, due to considerably lower data rates and more accessible sites (typically at sea level) that are linked to a high-speed internet backbone. The ngVLA reference design [33] also includes real-time data transport (320 Gbps per antenna) and correlation via ground fiber (both dedicated and leased commercial), even for the longest baselines spanning the United States and territories. However because the ngEHT operates a (comparatively) small number of antennas at remote locations spanning the globe, shipment of physical media is expected to remain the fastest and most economical method of transferring 100 s PB of data for the foreseeable future. Consistent array-wide high-speed internet access, such as that provided by global commercial Satellite RF internet, will nevertheless be extremely useful for rapid transfer of small amounts (∼1%) of data for interferometric validation and for obtaining near-realtime results where scientifically relevant.

The ngEHT is designed to operate full-season, and this motivates rapid processing and recycling of recording media to limit costs. Media are expected to be redeployed approximately once per two months (on average), versus once per 2–3 years as for the current EHT. As a result, there is less of a focus on media utility for economical long-term storage and more toward efficient recording and transport. Once data are brought to the correlation facility, they can be offloaded to local HDD-based storage if needed, for example, in the case of experiments including the South Pole Telescope which can incur several months of shipping delay. A rotating media library of 200 PB would be required to support a bimonthly turnaround of observations totaling 10 PB every three days while providing ample time for average shipping time and data offload.

6.2. Correlation

Correlation is the process of calculating pairwise correlation coefficients between the signals captured at each antenna. Because this is an operation on the PB of raw VLBI data, it is both I/O and computationally intensive and requires carefully matched computing platforms for effective processing. Correlation coefficients are typically calculated in the frequency domain using a so-called FX correlation architecture that enables efficient searching over unknown time delay via Fourier convolution. Frequency domain processing also allows for the convenient matching of signals from partially overlapping bandwidths as well as the application of linear and non-linear corrections to align the data. The consequences of an FX architecture is a large up-front cost to data channelization, scaling linearly with the number of antennas. For a 20-station network at ngEHT bandwidths, the $O(N)$ cost from data stream pre-processing and the $O(N^2)$ cost from calculating all pair-wise correlations are expected to be roughly comparable.

The current EHT records at 64 Gbps over 11 stations, for an aggregate rate of 0.7 Tbps. Data are correlated at dedicated computing clusters at MIT Haystack Observatory and the Max Planck Institute for Radioastronomy using the DiFX software correlator [101]. In aggregate, ∼2.5 k cores are able to process the full EHT bandwidth at about 10% real-time. Scaling linearly to the aggregate data rate of ngEHT requires ∼20 k cores to process ngEHT's ∼5 Tbps at 10% real-time (in comparison, 300 h of data per year, at 5 recorded hours per night on average, is a reasonable upper limit for ngEHT data throughput and reflects a duty cycle of 3.5% with respect to the total number of hours in a year). A quadratic scaling with the number of stations would imply double the requirement, but this can be balanced against ∼5–10% year-over-year improvements to single-core performance. CPU core density and efficiency are also increasing at a much faster rate, and GPU acceleration of both channelization and cross-multiply stages of correlation are expected to increase efficiency by another factor of ∼several. A detailed description and modeling of VLBI software correlation performance is presented in Vázquez et al. [102] alongside several benchmark results including those from the literature.

Approximately ∼60 M CPU core-hours would be required to correlate ∼680 PB (300 h) of raw data. VLBI data are taken non-continuously throughout the year and sometimes

require multiple passes through correlation to iterate on a proper configuration. Thus, is it necessary to over-provision on-demand computational resources by a factor of ∼few in order to avoid backlogs and ensure regular turnaround of recording media. Around ∼100 k on-demand CPU cores would be appropriate to keep up with the largest projected ngEHT data volumes, which is the size of a large institutional research cluster or a few medium-sized clusters distributed geographically. Due to the over-provisioning, the resources are ideally time-shared with other computing requirements (calibration and imaging, other VLBI correlation, or other general uses).

6.3. Calibration and Reduction

Output from correlation is at a resolution of ∼1 MHz in bandwidth and ∼1 second in time, which is required to capture residual instrumental and environmental systematics that affect the measured correlation coefficients such as lines, frequency response, relative delays, and time-varying gains and atmospheric phase [2,3]. These products are smaller than the recorded VLBI signals by a factor of $>10^3$ due to the large amount of accumulation following cross-correlation. A calibration process then solves for a refined instrument model and folds in any additional priors on the instrument response.

A key element of the calibration process is "fringe-fitting" where a parameterized phase model (typically relative *delay* and *delay-rate* over a short time interval) is self-calibrated to the correlator output. The fitting process verifies that a correlated signal exists in the data, measures the correlation coefficient, and allows data to be further coherently averaged, reducing the overall data volume by another factor of $\sim10^4$. Dedicated fringe fitting and calibration pipelines [93,103] were developed for EHT data to address the heterogeneous nature of the array and unique data properties. Compared to correlation, the computing requirements to fit a basic phase calibration model are low. For example, the EHT 2017 campaign data set (5 nights, 8 stations) can be processed through a multi-stage calibration and reduction pipeline using ∼1.5 k CPU core-hours [93].

This initial stage of calibration and reduction is aimed at reducing the overall data volume and complexity for downstream data products while applying only well-determined calibration solutions. Since data are manipulated and averaged, it is important to avoid introducing calibration solution noise or detailed assumptions about the source. In cases where calibration solutions are under-determined or degenerate with source model parameters, they must be jointly modeled during analysis. The complexity and computational cost can increase dramatically due to the high dimensionality of an instrument model, particularly in the case of formal Bayesian inference [104,105].

7. Instrumentation Design

In this section, we describe the basic elements of the ngEHT system (see Figure 12). These are the result of several internal project reviews, including a Systems Requirements Review, held on 9–10 June 2022. At this stage of the project, the ngEHT team has developed initial instrumental requirements through a process of preliminary trade-off analysis. This process has enabled the development of several prototypes, which have been selected for deployment in Phase 1 of the project, and these specific elements of the ngEHT system are described below.

7.1. Receiver

In Figure 13, (left), we present a block diagram of a dual-frequency receiver being constructed for ngEHT and to be deployed at the LMT. A single cryostat will hold two different receivers and the two different frequency bands are sent to each receiver through a frequency diplexer. Each receiver is dual-polarized, and features sideband separation mixers (see Table 4). Both bands illuminate a single beam in the sky, and the overall dual-frequency receiver has eight IF outputs, each of which is 4–12 GHz wide.

In an effort to make the design highly modular and scalable to reproduce for additional new telescopes of the ngEHT array, considerable effort has been invested into making the

mixer block compact and highly integrated. In Figure 13, (right), we show the components of this highly integrated block. Shown is a photo of the bottom block of a split-block mixer (bottom) and a schematic diagram of the components (top). A similar design will be employed for the 850 μm receiver as well. The 4 IF outputs from each of the mixer blocks are amplified cryogenically using commercially available low-noise amplifiers.

Each of the receiver bands is equipped with independent local-oscillator (LO) systems. YIG oscillators are lower frequencies (in the 18–30 GHz) range are multiplied up to the 3 mm wavelength band, and subsequently amplified using W-band power amplifiers. This is then fed through cryogenic triplers to produce the required LO signal. The drain currents of the last stage of the W-band power amplifiers can be adjusted to set the appropriate LO power for the mixers. The whole LO system is phase locked, and fully computer controlled with no mechanical moving parts.

Implementation of an additional 86 GHz capability to enable Frequency Phase Transfer (FPT) will proceed along multiple paths. For existing sites that already field 86 GHz receivers, these will be coupled where possible to higher frequency receivers using dichroics that enable simultaneous operation (e.g., GLT, JCMT). At existing sites that do not have 86 GHz receivers, or where existing 86 GHz systems cannot be used, new HEMT-based 86 GHz receivers, cooled to 20 K, will be added and coupled via dichroics. These new 86 GHz receivers will follow existing and proven designs. Finally, for the new ngEHT sites, a tri-band dewar that incorporates 86, 230, and 345 GHz receivers will be constructed, following existing designs and prototypes for the ongoing upgrade of the Submillimeter Array in Hawaii.
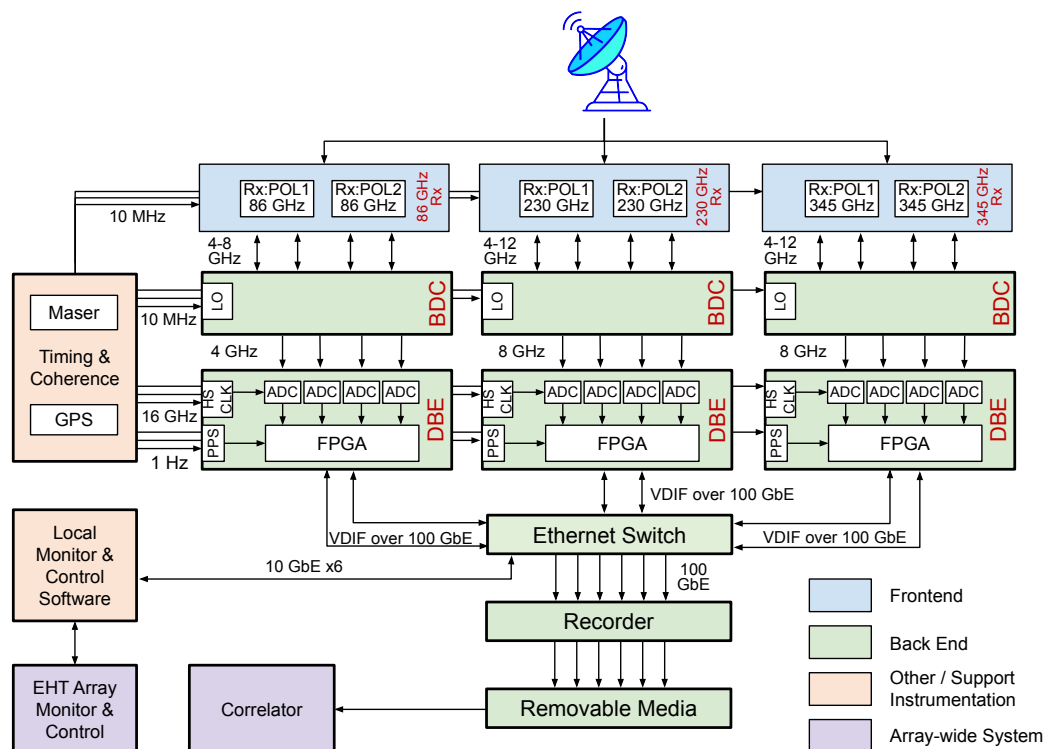
Figure 12. Functional block diagram of a next-generation EHT station. All elements shown in the figure are either commercially available (e.g., Hydrogen Maser), or in advanced prototyping stages, and suitable for deployment at ngEHT stations. The Timing & Coherence block consists of a Maser and GPS system, which provides ultra-stable clock signals for the DBE and references for the dual-polarization receivers and the BDC. A high-speed ethernet switch routes DBE packets to recorders with modular/removable media for shipment to the central correlator for interferometric processing. ngEHT Monitor and Control are handled by local and global systems.
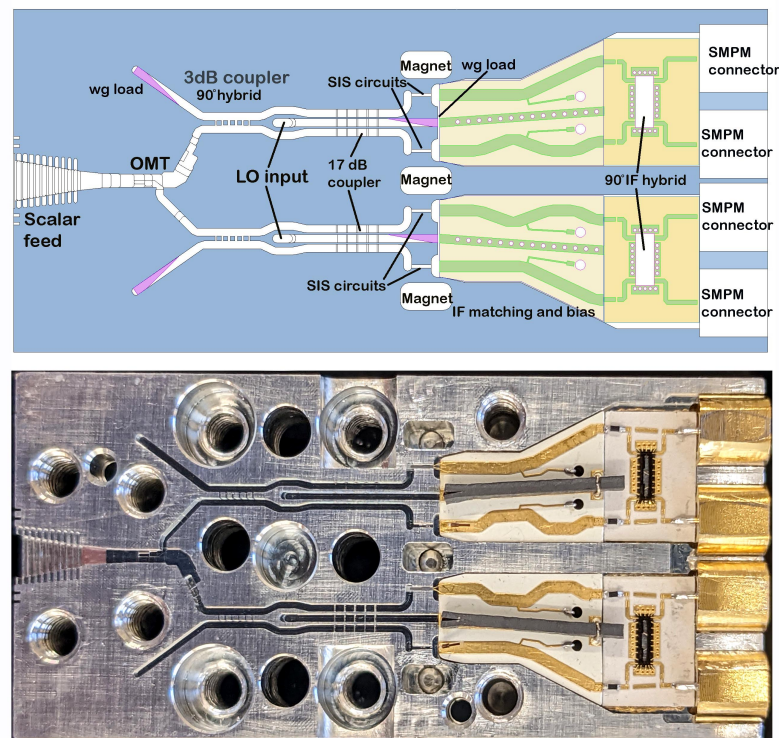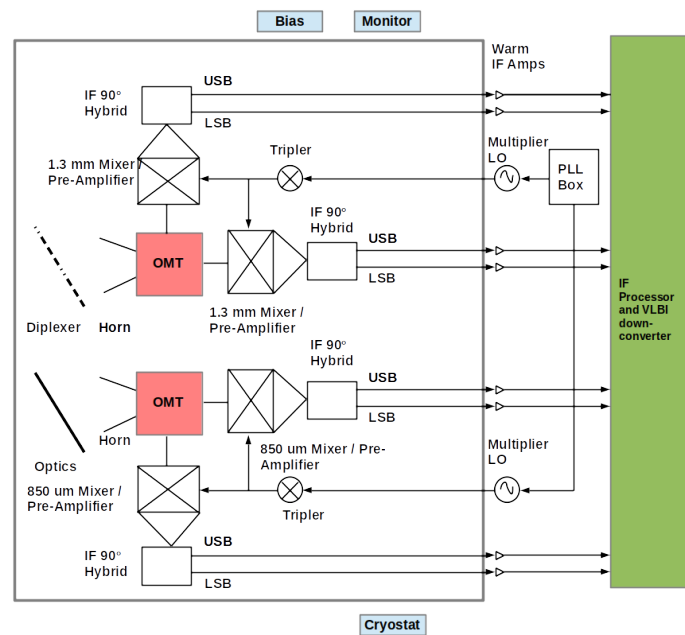
Figure 13. (**Top**) Block Diagram of the proposed dual-band SIS receivers. Both the 1.3 mm and 850 µm band receivers will be built inside a single cryostat. (**Middle**) Schematic outline of the 1.3 mm frontend receiver block. This block shows the cold section of the corrugated square feed-horn feeding an orthomode transducer (OMT) section that separates the input signal into two polarization channels, one in each of the top and bottom halves of the block. In each polarization, there is an RF 90° hybrid followed by LO couplers, ending in two SIS junctions. The IF outputs of the pair of SIS junctions pass through IF matching and bias tee to a superconducting IF 90° hybrid, which outputs the upper and lower sideband IF signals from that channel. In all 4 SIS junctions are used in each mixer block, with Cooper pair tunneling suppressed by permanent magnets. (**Bottom**) Photo of one half of an assembled 1.3 mm fronted receiver block.

Table 4. Specifications of the ngEHT multi-band Frequency Receiver.

Item	Description
3 mm RF Band	82–116 GHz
1 mm RF Band	210–280 GHz
850 µm RF Band	275–375 GHz
Polarizations	Dual pol in each band
Sidebands	2SB Receivers in each band
IF Frequency	4–12 GHz (1 mm, 0.85 µm)
	4–8 GHz (3 mm)
Receiver Noise	<50 K in 3 mm band
Temperature	60–70 K in 1 mm band
	70–80 K in 850 µm band

7.2. Backend

The ngEHT backend, consisting of the Block Down Converter (BDC) and the Digital BackEnd (DBE), will process twice the instantaneous bandwidth of the current EHT (reflecting the expansion of IF bandwidth from 4 GHz to 8 GHz).

The BDC performs a frequency translation and signal conditioning of the analog signal from the receivers. The Intermediate Frequency (IF) signal is converted to baseband, and output power levels are adjusted to optimally load the Analog to Digital Converter (ADC). The design of this BDC was initiated and functionality was implemented in a prototype, constructed by Xmicrowave LLC. The prototype was manufactured using drop-in PCB (Printed Circuit Board) modules instead of connected components, which is more representative of the final BDC PCB. A full characterization has been conducted and the results meet the required specifications. The final BDC will consist of integrated PCB units instead of discrete drop-ins.

The DBE prototype currently being used for testing and development is a two-board system. This prototype uses a custom circuit board holding four ADCs, which digitizes the analog signal from the BDC. This board sends the digital data stream to a commercial evaluation board, the VCU128 which houses the VU37P Field Programmable Gate Array (FPGA) from the Virtex Ultrascale+ family manufactured by Xilinx. Each 4-bit ADC is clocked at 16.384 GHz. The Nyquist bandwidth of this system is therefore 8.192 GHz, which is interoperable with the current EHT. The evaluation board is useful for current tests and development, and it will be replaced with a custom board design; the design of this new board is underway with an estimated one-year timeline to completion. Parts are being acquired to support a build of five units.

In addition to hardware (board) development, the initial firmware command set has been successfully completed, including an ADC interface module, a requantization block from 4 bits to 2 bits in the processing module, a packetization module, a 100 Gb transmission module, a Universal Asynchronous Receiver Transmitter(UART) monitor and control module, and a timing module. Further features that will be included in the firmware are channelization, 1 Gb monitor and control, and slope and ripple equalization.

With 2-bit quantization and Nyquist sampling, a single DBE can process the full IF bandwidth (8 GHz) from either the 1 mm or 0.85 mm band receiver, at a data rate of 128 Gb/s. For the 3 mm band, a narrower IF bandwidth (4 GHz) is sufficient to achieve Key Science Goals and Frequency Phase Transfer calibration. At 3 mm, the resulting data throughput is 64 Gb/s.

7.3. Recorder

The recorder is expected to be based around a set of commercial off-the-shelf (COTS) components hosted on a commodity multi-processor computer running a GNU/Linux operating system with a PCIe 4.0 interconnect. A single recording unit is matched to one or more streams from the digital back-end system (DBE), which is designed to output 64 Gbps data streams on 100 GbE interconnect using the VDIF transport protocol (VTP, [106])

over UDP. Specialized software on the recording unit provides efficient network capture at the required rates, simple packet inspection to ensure data continuity and integrity, distributed writing of VDIF file streams to disk, and an interface to the VLBI monitor and control system.

The host recording system will buffer the incoming data in system RAM, while simultaneously draining this data to persistent memory for storage. The persistent storage is expected to be a set of solid-state drives (SSDs) attached via PCIe/NVMe (integrated media). The total number, individual capacity and write performance of the component SSDs in the persistent memory pool will be selected such that they are sufficient to absorb the total aggregate data rate and meet the desired overall capacity and cost constraints. In order to facilitate playback of detachable data modules for subsequent correlation or transfer, the recorder will maintain a file system on the media so that may be mounted by separate machine. Comparison of specifications for the current Mark6 recorders used in the EHT and an ngRecorder is shown in Table 5.

Table 5. Specifications for a modular VLBI recorder, including those of the Mark6 [107] currently in use across the EHT. Reference specifications for a next-generation SSD-based recorder are based on common currently available COTS SSD storage servers.

	Mark6	ngRecorder
rack space	11U	2U
disks	32 HDD	24 SSD
capacity	512 TB	369 TB
interface	$4 \times 10/25$ GbE	2×100 GbE
rate	16/32 Gbps	128 Gbps
hours at rate	71.1/35.6	6.4
disk modules	yes	no

Although an SSD-based recorder has several advantages over an HDD-based system in terms of speed, power, density, weight, and latency, SSDs are anticipated to carry a significant cost premium to HDDs for the next decade. Moreover, a modular removable disk pack system analogous to the semi-custom Mark6 module [107] has yet to be designed, which limits the flexibility of current COTS SSD recorders. For this reason, large volume data storage and possibly transport may still rely on HDD-based solutions for some time, with SSD-to-HDD data offload capability at the site or at the correlator.

7.4. Array Monitoring and Control

The operations concept for the ngEHT extends beyond the single annual campaign of the current EHT:

- 60 nights of observing per year
- Up to 21 stations observing simultaneously
- Varied observation cadences and durations throughout the year
- Readiness for VLBI observing in 24 h or less to capture ToOs
- Multi-messenger campaigns
- Configurable subarrays
- As much remote operation as possible

This model and its increase in capability have a direct impact on the requirements and subsequent complexity of the M&C system for the ngEHT. As the M&C system serves as a main interface point for operations of the array, its design must be operator-centered and have due consideration for human factors concerns. As well, the operations concept is designed to address an explicit need, voiced at the ngEHT Operations Workshop (31 March 2022), to reduce the burden (relative to 2022 EHT operations) for on-site monitoring, control, and maintenance of VLBI equipment. The areas to address include differing methods of monitoring and control for each station and heavy reliance on local operations at each site, including the need for VLBI specialists on site.

As the first ngEHT sites are brought online, they will participate in the annual EHT observing campaign. To facilitate this participation, the M&C system will be compatible with the EHT operations plans and procedures by relaying data to the existing VLBI Monitor server, providing remote control of station subsystems, and providing status, logs, and metadata as required. Outside of the annual EHT campaign, the ngEHT operations concept calls for an annual monitoring campaign where the M&C system will be used to operate and monitor the entire array. It will provide a uniform and cohesive monitoring and control experience to the array operators while managing a heterogeneous array of ngEHT stations and stations that use the existing EHT VM&C system and backend equipment.

Collecting observation metadata from a heterogeneous array of telescopes that have non-standardized interfaces for M&C and data collection is a significant design and operational challenge. To take advantage of the opportunity presented by the ngEHT designing its own telescopes, it is expected that the M&C component of the telescopes for ngEHT sites will be designed in conjunction with the overall M&C system to make this interface as common as possible across the ngEHT sites.

As the number of stations and observations grows, providing on-site VLBI expertise will become increasingly challenging. The ngEHT design approach follows an operations model where station operators can remotely perform any required operations and maintenance, with specialist support being provided only when necessary. Remote operation is facilitated by the focus on human factors and operator-centered design, and leads to less reliance on manual operations and analysis. A cloud-based deployment of the array-level M&C system is envisioned as the way to provide "operations from anywhere" capability to the array operations staff. This is expected to include a server, database, and UI components that facilitate operation of the array. M&C capability at each station is still required to provide the control inputs to station subsystems and aggregate the local data for relay to the array-level system. Remote access to both the array- and station-level M&C systems are provided with appropriate security, authentication, and authorization methods.

To achieve all this, the M&C system architecture is expected to be built from off-the-shelf software components using open standards, including databases, message queueing and information exchange methods, and operator interface frameworks. This facilitates development and maintenance over the lifecycle of the array. A robustly defined software architecture allows isolation of site-specific dependencies to the smallest and fewest components necessary.

7.5. Antennas

The ngEHT concept adds ∼10 new antennas to the existing EHT array. In Phase 1 the ngEHT program will deploy 3–4 modest-diameter antennas for the most rapid increase in next-generation science (see Section 4.4). To mitigate risk, the program has identified two possible paths toward this Phase 1 enhancement. The first would use three 6 m diameter antennas from the decommissioned Berkeley-Illinois-Maryland-Array (BIMA), which would be transported to the Las Campanas (LCO), San Pedro Martir (SPM), and Canary Island (CNI) sites.

The BIMA dishes have a surface accuracy specification of ∼40 μm rms, sufficient for operation up to 345 GHz. Photogrammetry measurements will allow re-adjustment the surface to the required accuracy after re-assembly of the antenna. The panels of all three dishes are in good condition, as shown in Figure 14.

Figure 2 suggests that a 6 m diameter antenna with an aperture efficiency of 0.8 would allow us to reach the required sensitivity when paired with a large collecting area dish such as LMT or phased ALMA. But a larger diameter antenna will relax the requirement on long-distance baselines away from such anchor stations, and also have two additional advantages: easier calibration for pointing and focus measurements, and ability to carry out single-dish science projects while the antennas are not observing for ngEHT in VLBI mode.

Therefore, a second possible Phase 1 implementation path would be to use newly fabricated dishes of 9 m diameter. The specifications of the new antennas are summarized

in Table 6. The ngEHT team is in discussions with several telescope vendors and it is clear that dishes with the required specifications can be procured within a reasonable cost envelope. In this case, Phase 1 would target four sites: the Mt. Jelm site in Wyoming (JELM), in addition to Canary Islands (CNI), San Pedro Martir (SPM), and Las Campanas (LCO).

Figure 14. Photograph showing the condition of the BIMA antenna dish surface (from March 2022).

Table 6. Specifications of the new ngEHT antennas.

Design Specifications	
Primary reflector diameter	9 m
Mount architecture	Alt-Az
Optics	Cassegrain
Sun avoidance zone	None
Operating Specifications	
Surface accuracy	30 μm rms
Frequency range	86–345 GHz
Aperture efficiency	0.8
Pointing accuracy	2″ rms (all sky, blind)
Tracking accuracy	0.2″
Aperture blockage	<5%
Gain variation with elevation	<5%
Range of motion in azimuth	−180°–360°,
Range of motion in elevation	3°–90°,
Slew speed	1°/s
Environmental Specifications	
Temperature	−15 to +35 °C operational
	−20 to +45 °C high
	−30 to +55 °C survival
Wind speed	10 m/s operational
	15 m/s high
	50 m/s survival

8. Summary and Conclusions

The ngEHT, described initially to the Astro2020 decadal survey review [39], is a program to plan extensions of the EHT array that will deliver high dynamic range imaging and movie-making capability for black hole studies on event horizon scales. It does so principally by deploying modest-diameter radio dishes at optimized geographical locations, which significantly increases interferometric baseline coverage (Figures 8–10), by implementing a simultaneous tri-band (86, 230, 345 GHz) receiver suite, and increasing the bandwidth of backend systems and data processing pipelines.

The process and initial results of optimizing site selection for ngEHT telescopes described here indicate two possible paths to achieve a next-generation EHT array.

In the first path, Phase 1 consists of adding dishes at two existing sites (OVRO and Haystack) to the current EHT, and available refurbished dishes from the BIMA array would be relocated to three sites (Las Campanas, Chile; San Pedro Martir, Mexico; Canary Islands, Spain). Then in Phase 2, additional sites would be developed; current analysis indicates that the combination of these locations: La Paz, Bolivia; Wyoming, US; Marangu, Tanzania; Santiago, Chile; and Bern, Switzerland, constitute an array that can deliver all of the threshold Key Science Goals. These Phase 2 sites should be considered possibilities at this stage; more work is required to assess them at all levels, including thorough consideration of cultural and environmental aspects.

In an alternate path, Phase 1 would again add both OVRO and Haystack to the EHT, and four new 9 m diameter dishes would be deployed to the Mt. Jelm site in Wyoming; Las Campanas, Chile; San Pedro Martir, Mexico; and Canary Islands, Spain. Then in Phase 2, planned new telescopes are added to the array as they become available, including the AMT, LLAMA and KVNYS, KVNPC facilities. Either of these approaches to realizing the ngEHT leads to the increases in global array capabilities that are required to achieve all ngEHT Key Science Goals.

Strategies for ngEHT data transport, correlation, calibration, and data reduction are all developed. Requirements for major instrumental sub-systems are specified, and details of prototypes to be used are described. In sum, this work brings the ngEHT project to the point of readiness for implementation.

Appendix A. Additional Site Selection Details

Table A1 lists the sites considered for the ngEHT array optimization procedures described in Section 4. This pool of candidate sites has been taken from [86], and they have been selected for their favorable atmospheric transmission properties at 230 GHz and 345 GHz during the typical EHT observing season in March and April.

Table A2 specifies the pre-existing arrays assumed during the site selection procedure described in Section 4. Four different variants of pre-existing array are explored as parameters in the site selection procedure, and these variants are enumerated in the table.

Table A1. Existing or planned sites (top) and candidate ngEHT sites (bottom), updated from [86].

Site Code	Location	Latitude	Longitude	Elevation (m)
ALMA	Atacama, Chile	−23.032	−67.755	5040
AMT	Gamsberg, Namibia	−23.339	16.229	2340
APEX	Atacama, Chile	−23.005	−67.759	5060
GLT	Pituffik Space Base, Greenland	76.535	−68.686	70
HAY	Westford, Massachusetts, USA	42.624	−71.489	110
IRAM	Sierra Nevada, Spain	37.066	−3.393	2860
JCMT	Mauna Kea, Hawaii	19.823	−155.477	4070
KP	Arizona, USA	31.953	−111.615	1930
KVNPC	Pyeongchang, South Korea	37.534	128.450	500
KVNYS	Yonsei, South Korea	37.565	126.941	90
LLA	Salta, Argentina	−24.192	−66.475	4780
LMT	Sierra Negra, Mexico	18.986	−97.315	4620
NOEMA	Plateau de Bure, France	44.634	5.907	2550
OVRO	California, USA	37.231	−118.282	1210
SMA	Mauna Kea, Hawaii	19.824	−155.478	4070
SMT	Arizona, USA	32.702	−109.891	3170
SPT	South Pole, Antarctica	−90	0	2820
ALI	Hotan County, China	35.963	79.338	6080
BAN	Alberta, Canada	51.350	−116.206	3470
BAR	California, USA	37.634	−118.256	4340
BGA	Progled, Bulgaria	41.695	24.738	1730
BGK	Westfjords, Iceland	66.032	−23.052	830
BLDR	Colorado, USA	39.588	−105.643	4340
BMAC	Eastern Cape, South Africa	−31.096	27.889	2420
BOL	La Paz, Bolivia	−16.351	−68.131	5230
BRZ	Espírito Santo, Brazil	−20.439	−41.799	2850
CAS	Tierra del Fuego, Argentina	−54.790	−68.415	2850
CAT	Río Negro, Argentina	−41.170	−71.486	2100
CNI	La Palma, Canary Islands	28.299	−16.509	2360
DomeA	Upper ice sheet, Antarctica	−80.367	77.351	4090
DomeC	Upper ice sheet, Antarctica	−75.101	123.342	3230
DomeF	Upper ice sheet, Antarctica	−77.317	39.702	3700
ERB	Khalifan, Iraq	36.584	44.466	2110
FAIR	Alaska, USA	64.988	−147.599	620
FLWO	Arizona, USA	31.675	−110.951	1270
FUJI	Fujinomiya & Yamanashi, Japan	35.367	138.730	3750
GARS	Trinity Peninsula, Antarctica	−63.320	−57.895	20
GLTS	Ice sheet summit, Greenland	72.580	−38.449	3230
HAN	Ladakh, India	32.780	78.963	4500
JELM	Wyoming, USA	41.097	−105.977	2940
KEN	Meru, Kenya	−0.141	37.315	4260
KILI	Kilimanjaro, Tanzania	−3.088	37.406	4430
LCO	Coquimbo, Chile	−29.032	−70.685	2320
LOS	New Mexico, USA	35.880	−106.675	2000
NOB	Nagano, Japan	35.944	138.472	1370
NZ	Canterbury, New Zealand	−43.987	170.465	1010
ORG	Oregon, USA	42.635	−118.576	2970
PAR	Antofagasta, Chile	−24.628	−70.404	2640
PIKE	Colorado, USA	38.841	−105.041	4280
SAN	California, USA	34.099	−116.825	3500
SGO	Santiago, Chile	−33.3346	−70.270	3350

Table A1. *Cont.*

Site Code	Location	Latitude	Longitude	Elevation (m)
SKS	Crete, Greece	35.212	24.898	1740
SPM	Baja California, Mexico	31.045	−115.464	2800
SPX	Fieschertal, Switzerland	46.548	7.985	3510
SUF	Zaamin, Uzbekistan	39.623	68.468	2440
TRL	Jutulsessen, Antarctica	−72.010	2.540	1280
VLA	New Mexico, USA	34.079	−107.618	2120
YAN	Huanca Sancos, Peru	−13.938	−74.392	4230
YBG	Lhasa Tibet, China	30.006	91.027	5360

Table A2. The different pre-existing arrays considered as part of the site selection exploration (Section 4.4). Each of these combinations of stations is the starting set of sites for which the addition of three sites (for the Phase 1 analysis) or five sites (for the Phase 2 analysis) are explored. These starting arrays are chosen to generally represent the possible operating modes shown in Table 3. Set 1, for example, might be a minimal array useful for Target of Opportunity observations. Sets 2 and 3, with the addition of a large aperture, could provide flexible long-term monitoring capability. And set 4 includes all possible stations for a full campaign mode. The range of starting arrays also give some indication of optimal placement in the full campaign mode in the case where some sites are not available due to weather or technical issues.

Parameter Set	Pre-Existing Stations from EHT Array	Other Pre-Existing Stations Assumed
Phase 1 set 1	none	HAY, OVRO
Phase 1 set 2	LMT	HAY, OVRO
Phase 1 set 3	APEX, GLT, JCMT, LMT, SMT	HAY, OVRO
Phase 1 set 4	ALMA, APEX, GLT, IRAM, JCMT, KP, LMT, NOEMA, SMA, SMT, SPT	HAY, OVRO
Phase 2 set 1	none	CNI, HAY, LCO, OVRO, SPM
Phase 2 set 2	LMT	CNI, HAY, LCO, OVRO, SPM
Phase 2 set 3	APEX, GLT, JCMT, LMT, SMT	CNI, HAY, LCO, OVRO, SPM
Phase 2 set 4	ALMA, APEX, GLT, IRAM, JCMT, KP, LMT, NOEMA, SMA, SMT, SPT	CNI, HAY, LCO, OVRO, SPM

Notes

[1]   Available online: https://www.mdpi.com/journal/galaxies/special_issues/ngEHT_blackholes (accessed on 16 August 2023).

[2]   Available online: https://github.com/Smithsonian/ngehtsim (accessed on 16 August 2023).

[3]   Available online: https://www.evlbi.org/ (accessed on 16 August 2023).

References

1.   Akiyama, K. et al. [Event Horizon Telescope Collaboration]. First M87 Event Horizon Telescope Results. I. The Shadow of the Supermassive Black Hole. *Astrophys. J. Lett.* **2019**, *875*, L1. [CrossRef]

2.   Akiyama, K. et al. [Event Horizon Telescope Collaboration]. First M87 Event Horizon Telescope Results. II. Array and Instrumentation. *Astrophys. J. Lett.* **2019**, *875*, L2. [CrossRef]

3.   Akiyama, K. et al. [Event Horizon Telescope Collaboration]. First M87 Event Horizon Telescope Results. III. Data Processing and Calibration. *Astrophys. J. Lett.* **2019**, *875*, L3. [CrossRef]

4.   Akiyama, K. et al. [Event Horizon Telescope Collaboration]. First M87 Event Horizon Telescope Results. IV. Imaging the Central Supermassive Black Hole. *Astrophys. J. Lett.* **2019**, *875*, L4. [CrossRef]

5.   Akiyama, K. et al. [Event Horizon Telescope Collaboration]. First M87 Event Horizon Telescope Results. V. Physical Origin of the Asymmetric Ring. *Astrophys. J. Lett.* **2019**, *875*, L5. [CrossRef]

6.   Akiyama, K. et al. [Event Horizon Telescope Collaboration]. First M87 Event Horizon Telescope Results. VI. The Shadow and Mass of the Central Black Hole. *Astrophys. J. Lett.* **2019**, *875*, L6. [CrossRef]

7.   Akiyama, K. et al. [Event Horizon Telescope Collaboration]. First Sagittarius A* Event Horizon Telescope Results. I. The Shadow of the Supermassive Black Hole in the Center of the Milky Way. *Astrophys. J. Lett.* **2022**, *930*, L12. [CrossRef]

8.   Akiyama, K. et al. [Event Horizon Telescope Collaboration]. First Sagittarius A* Event Horizon Telescope Results. II. EHT and Multiwavelength Observations, Data Processing, and Calibration. *Astrophys. J. Lett.* **2022**, *930*, L13. [CrossRef]

9.   Akiyama, K. et al. [Event Horizon Telescope Collaboration]. First Sagittarius A* Event Horizon Telescope Results. III. Imaging of the Galactic Center Supermassive Black Hole. *Astrophys. J. Lett.* **2022**, *930*, L14. [CrossRef]

10.   Akiyama, K. et al. [Event Horizon Telescope Collaboration]. First Sagittarius A* Event Horizon Telescope Results. IV. Variability, Morphology, and Black Hole Mass. *Astrophys. J. Lett.* **2022**, *930*, L15. [CrossRef]

11. Akiyama, K. et al. [Event Horizon Telescope Collaboration]. First Sagittarius A* Event Horizon Telescope Results. V. Testing Astrophysical Models of the Galactic Center Black Hole. *Astrophys. J. Lett.* **2022**, *930*, L16. [CrossRef]

12. Akiyama, K. et al. [Event Horizon Telescope Collaboration]. First Sagittarius A* Event Horizon Telescope Results. VI. Testing the Black Hole Metric. *Astrophys. J. Lett.* **2022**, *930*, L17. [CrossRef]

13. Bardeen, J.M. Timelike and null geodesics in the Kerr metric. In *Black Holes (Les Astres Occlus)*; Gordon and Breach: New York, NY, USA, 1973; pp. 215–239.

14. Luminet, J.P. Image of a spherical black hole with thin accretion disk. *Astron. Astrophys.* **1979**, *75*, 228–235.

15. Falcke, H.; Melia, F.; Agol, E. Viewing the Shadow of the Black Hole at the Galactic Center. *Astrophys. J. Lett.* **2000**, *528*, L13–L16. [CrossRef]

16. Takahashi, R. Shapes and Positions of Black Hole Shadows in Accretion Disks and Spin Parameters of Black Holes. *Astrophys. J.* **2004**, *611*, 996–1004. [CrossRef]

17. Broderick, A.E.; Loeb, A. Imaging optically-thin hotspots near the black hole horizon of Sgr A* at radio and near-infrared wavelengths. *Mon. Not. R. Astron. Soc.* **2006**, *367*, 905–916. [CrossRef]

18. Padin, S.; Woody, D.P.; Hodges, M.W.; Rogers, A.E.E.; Emerson, D.T.; Jewell, P.R.; Lamb, J.; Perfetto, A.; Wright, M.C.H. 223 GHz VLBI Observations of 3C 273. *Astrophys. J. Lett.* **1990**, *360*, L11. [CrossRef]

19. Krichbaum, T.P.; Graham, D.A.; Witzel, A.; Greve, A.; Wink, J.E.; Grewing, M.; Colomer, F.; de Vicente, P.; Gomez-Gonzalez, J.; Baudry, A.; et al. VLBI observations of the galactic center source SGR A* at 86 GHz and 215 GHz. *Astron. Astrophys.* **1998**, *335*, L106–L110.

20. Doeleman, S.S.; Weintroub, J.; Rogers, A.E.E.; Plambeck, R.; Freund, R.; Tilanus, R.P.J.; Friberg, P.; Ziurys, L.M.; Moran, J.M.; Corey, B.; et al. Event-horizon-scale structure in the supermassive black hole candidate at the Galactic Centre. *Nature* **2008**, *455*, 78–80. [CrossRef]

21. Doeleman, S.S.; Fish, V.L.; Schenck, D.E.; Beaudoin, C.; Blundell, R.; Bower, G.C.; Broderick, A.E.; Chamberlin, R.; Freund, R.; Friberg, P.; et al. Jet-Launching Structure Resolved Near the Supermassive Black Hole in M87. *Science* **2012**, *338*, 355. [CrossRef]

22. Fish, V.L.; Doeleman, S.S.; Beaudoin, C.; Blundell, R.; Bolin, D.E.; Bower, G.C.; Chamberlin, R.; Freund, R.; Friberg, P.; Gurwell, M.A.; et al. 1.3 mm Wavelength VLBI of Sagittarius A*: Detection of Time-variable Emission on Event Horizon Scales. *Astrophys. J. Lett.* **2011**, *727*, L36. [CrossRef]

23. Johnson, M.D.; Fish, V.L.; Doeleman, S.S.; Marrone, D.P.; Plambeck, R.L.; Wardle, J.F.C.; Akiyama, K.; Asada, K.; Beaudoin, C.; Blackburn, L.; et al. Resolved magnetic-field structure and variability near the event horizon of Sagittarius A*. *Science* **2015**, *350*, 1242–1245. [CrossRef]

24. Doeleman, S.; Agol, E.; Backer, D.; Baganoff, F.; Bower, G.C.; Broderick, A.; Fabian, A.; Fish, V.; Gammie, C.; Ho, P.; et al. Imaging an Event Horizon: Submm-VLBI of a Super Massive Black Hole. *arXiv* **2009**, arXiv:0906.3899.

25. Doeleman, S. Building an event horizon telescope: (sub)mm VLBI in the ALMA era. In Proceedings of the 10th European VLBI Network Symposium and EVN Users Meeting: VLBI and the New Generation of Radio Arrays, Manchester, UK, 20–24 September 2010; p. 53.

26. Matthews, L.D.; Crew, G.B.; Doeleman, S.S.; Lacasse, R.; Saez, A.F.; Alef, W.; Akiyama, K.; Amestica, R.; Anderson, J.M.; Barkats, D.A.; et al. The ALMA Phasing System: A Beamforming Capability for Ultra-high-resolution Science at (Sub)Millimeter Wavelengths. *Publ. Astron. Soc. Pac.* **2018**, *130*, 015002. [CrossRef]

27. Inoue, M.; Algaba-Marcos, J.C.; Asada, K.; Blundell, R.; Brisken, W.; Burgos, R.; Chang, C.C.; Chen, M.T.; Doeleman, S.S.; Fish, V.; et al. Greenland telescope project: Direct confirmation of black hole with sub-millimeter VLBI. *Radio Sci.* **2014**, *49*, 564–571. [CrossRef]

28. Kim, J.; Marrone, D.P.; Beaudoin, C.; Carlstrom, J.E.; Doeleman, S.S.; Folkers, T.W.; Forbes, D.; Greer, C.H.; Lauria, E.F.; Massingill, K.D.; et al. A VLBI receiving system for the South Pole Telescope. In *Millimeter, Submillimeter, and Far-Infrared Detectors and Instrumentation for Astronomy IX*; Society of Photo-Optical Instrumentation Engineers (SPIE) Conference Series; Zmuidzinas, J., Gao, J.R., Eds.; SPIE: Bellingham, WA, USA, 2018; Volume 10708, p. 107082S.

29. Christensen, L.L.; Baloković, M.; Chou, M.Y.; Crowley, S.; Edmonds, P.; Foncea, V.; Hiramatsu, M.; Hunter, C.; Königstein, K.; Leach, S.; et al. An Unprecedented Global Communications Campaign for the Event Horizon Telescope First Black Hole Image. *Commun. Astron. Public J.* **2019**, *26*, 11.

30. Vertatschitsch, L.; Primiani, R.; Young, A.; Weintroub, J.; Crew, G.B.; McWhirter, S.R.; Beaudoin, C.; Doeleman, S.; Blackburn, L. R2DBE: A Wideband Digital Backend for the Event Horizon Telescope. *Publ. Astron. Soc. Pac.* **2015**, *127*, 1226. [CrossRef]

31. Carpenter, J.; Iono, D.; Kemper, F.; Wootten, A. The ALMA Development Program: Roadmap to 2030. *arXiv* **2020**, arXiv:2001.11076.

32. Grimes, P.; Blundell, R.; Leiker, P.; Paine, S.N.; Tong, E.C.Y.; Wilson, R.W.; Zeng, L. Receivers for the Wideband Submillimeter Array. In Proceedings of the 31st International Symposium on Space Terahertz Technology, Tempe, AZ, USA, 8–11 March 2020; pp. 60–66.

33. Selina, R.J.; Murphy, E.J.; McKinnon, M.; Beasley, A.; Butler, B.; Carilli, C.; Clark, B.; Durand, S.; Erickson, A.; Grammer, W.; et al. The ngVLA Reference Design. In *Science with a Next Generation Very Large Array*; Astronomical Society of the Pacific Conference Series; Murphy, E., Ed.; ASP: San Francisco, CA, USA, 2018; Volume 517, p. 15. [CrossRef]

34. Selina, R.; Murphy, E.; Beasley, A. The ngVLA: A technical development update. In *Ground-Based and Airborne Telescopes IX*; Marshall, H.K., Spyromilio, J., Usuda, T., Eds.; International Society for Optics and Photonics, SPIE: Bellingham, WA, USA, 2022; Volume 12182, p. 1218200. [CrossRef]

35. Gill, A.; Blackburn, L.; Roshanineshat, A.; Chan, C.K.; Doeleman, S.S.; Johnson, M.D.; Raymond, A.W.; Weintroub, J. Prospects for Wideband VLBI Correlation in the Cloud. *Publ. Astron. Soc. Pac.* **2019**, *131*, 124501. [CrossRef]

36. Johnson, M.D.; Bouman, K.L.; Blackburn, L.; Chael, A.A.; Rosen, J.; Shiokawa, H.; Roelofs, F.; Akiyama, K.; Fish, V.L.; Doeleman, S.S. Dynamical Imaging with Interferometry. *Astrophys. J.* **2017**, *850*, 172. [CrossRef]

37. Bouman, K.L.; Johnson, M.D.; Dalca, A.V.; Chael, A.A.; Roelofs, F.; Doeleman, S.S.; Freeman, W.T. Reconstructing Video of Time-Varying Sources From Radio Interferometric Measurements. *IEEE Trans. Comput. Imaging* **2018**, *4*, 512–527. [CrossRef]

38. Arras, P.; Frank, P.; Haim, P.; Knollmüller, J.; Leike, R.; Reinecke, M.; Enßlin, T. Variable structures in M87* from space, time and frequency resolved interferometry. *Nat. Astron.* **2022**, *6*, 259–269. [CrossRef]

39. Doeleman, S.; Blackburn, L.; Dexter, J.; Gomez, J.L.; Johnson, M.D.; Palumbo, D.C.; Weintroub, J.; Farah, J.R.; Fish, V.; Loinard, L.; et al. Studying Black Holes on Horizon Scales with VLBI Ground Arrays. *arXiv* **2019**, arXiv:1909.01411.

40. National Academies of Sciences, Engineering, and Medicine. *Pathways to Discovery in Astronomy and Astrophysics for the 2020s*; The National Academies Press: Washington, DC, USA, 2021. [CrossRef]

41. Chael, A.; Issaoun, S.; Pesce, D.w.; Johnson, M.D.; Ricarte, A.; Fromm, C.M.; Mizuno, Y. Multi-frequency Black Hole Imaging for the Next-Generation Event Horizon Telescope. *arXiv* **2022**, arXiv:2210.12226.

42. Crew, G.B.; Goddi, C.; Matthews, L.D.; Rottmann, H.; Saez, A.; Martí-Vidal, I. A Characterization of the ALMA Phasing System at 345 GHz. *Publ. Astron. Soc. Pac.* **2023**, *135*, 025002. [CrossRef]

43. Rioja, M.J.; Dodson, R.; Asaki, Y. The Transformational Power of Frequency Phase Transfer Methods for ngEHT. *Galaxies* **2023**, *11*, 16. [CrossRef]

44. Issaoun, S.; Pesce, D.W.; Roelofs, F.; Chael, A.; Dodson, R.; Rioja, M.J.; Akiyama, K.; Aran, R.; Blackburn, L.; Doeleman, S.S.; et al. Enabling Transformational ngEHT Science via the Inclusion of 86 GHz Capabilities. *Galaxies* **2023**, *11*, 28. [CrossRef]

45. Kauffmann, J.; Rajagopalan, G.; Akiyama, K.; Fish, V.; Lonsdale, C.; Matthews, L.D.; Pillai, T.G. The Haystack Telescope as an Astronomical Instrument. *Galaxies* **2023**, *11*, 9. [CrossRef]

46. Johnson, M.D.; Akiyama, K.; Blackburn, L.; Bouman, K.L.; Broderick, A.E.; Cardoso, V.; Fender, R.P.; Fromm, C.M.; Galison, P.; Gómez, J.L.; et al. Key Science Goals for the Next-Generation Event Horizon Telescope. *Galaxies* **2023**, *11*, 61. [CrossRef]

47. Chael, A.; Johnson, M.D.; Lupsasca, A. Observing the Inner Shadow of a Black Hole: A Direct View of the Event Horizon. *Astrophys. J.* **2021**, *918*, 6. [CrossRef]

48. Dokuchaev, V.I.; Nazarova, N.O. Event Horizon Image within Black Hole Shadow. *Sov. J. Exp. Theor. Phys.* **2019**, *128*, 578–585. [CrossRef]

49. Palumbo, D.C.M.; Wong, G.N.; Prather, B.S. Discriminating Accretion States via Rotational Symmetry in Simulated Polarimetric Images of M87. *Astrophys. J.* **2020**, *894*, 156. [CrossRef]

50. Ricarte, A.; Tiede, P.; Emami, R.; Tamar, A.; Natarajan, P. The ngEHT's Role in Measuring Supermassive Black Hole Spins. *Galaxies* **2023**, *11*, 6. [CrossRef]

51. Pesce, D.W.; Palumbo, D.C.M.; Narayan, R.; Blackburn, L.; Doeleman, S.S.; Johnson, M.D.; Ma, C.P.; Nagar, N.M.; Natarajan, P.; Ricarte, A. Toward Determining the Number of Observable Supermassive Black Hole Shadows. *Astrophys. J.* **2021**, *923*, 260. [CrossRef]

52. Pesce, D.W.; Palumbo, D.C.M.; Ricarte, A.; Broderick, A.E.; Johnson, M.D.; Nagar, N.M.; Natarajan, P.; Gómez, J.L. Expectations for Horizon-Scale Supermassive Black Hole Population Studies with the ngEHT. *Galaxies* **2022**, *10*, 109. [CrossRef]

53. Ramakrishnan, V.; Nagar, N.; Arratia, V.; Hernández-Yévenes, J.; Pesce, D.W.; Nair, D.G.; Bandyopadhyay, B.; Medina-Porcile, C.; Krichbaum, T.P.; Doeleman, S.; et al. Event Horizon and Environs (ETHER): A Curated Database for EHT and ngEHT Targets and Science. *Galaxies* **2023**, *11*, 15. [CrossRef]

54. Balbus, S.A.; Hawley, J.F. Instability, turbulence, and enhanced transport in accretion disks. *Rev. Mod. Phys.* **1998**, *70*, 1–53. [CrossRef]

55. Yuan, F.; Narayan, R. Hot Accretion Flows Around Black Holes. *Annu. Rev. Astron. Astrophys.* **2014**, *52*, 529–588. [CrossRef]

56. Rowan, M.E.; Sironi, L.; Narayan, R. Electron and Proton Heating in Transrelativistic Magnetic Reconnection. *Astrophys. J.* **2017**, *850*, 29. [CrossRef]

57. Ball, D.; Sironi, L.; Özel, F. Electron and Proton Acceleration in Trans-relativistic Magnetic Reconnection: Dependence on Plasma Beta and Magnetization. *Astrophys. J.* **2018**, *862*, 80. [CrossRef]

58. Blandford, R.D.; Znajek, R.L. Electromagnetic extraction of energy from Kerr black holes. *Mon. Not. R. Astron. Soc.* **1977**, *179*, 433–456. [CrossRef]

59. Tchekhovskoy, A.; Narayan, R.; McKinney, J.C. Efficient generation of jets from magnetically arrested accretion on a rapidly spinning black hole. *Mon. Not. R. Astron. Soc.* **2011**, *418*, L79–L83. [CrossRef]

60. Blandford, R.; Meier, D.; Readhead, A. Relativistic Jets from Active Galactic Nuclei. *Annu. Rev. Astron. Astrophys.* **2019**, *57*, 467–509. [CrossRef]

61. Johnson, M.D.; Lupsasca, A.; Strominger, A.; Wong, G.N.; Hadar, S.; Kapec, D.; Narayan, R.; Chael, A.; Gammie, C.F.; Galison, P.; et al. Universal interferometric signatures of a black hole's photon ring. *Sci. Adv.* **2020**, *6*, eaaz1310. [CrossRef]

62. Tiede, P.; Johnson, M.D.; Pesce, D.W.; Palumbo, D.C.M.; Chang, D.O.; Galison, P. Measuring Photon Rings with the ngEHT. *Galaxies* **2022**, *10*, 111. [CrossRef]

63. Vincent, F.H.; Gralla, S.E.; Lupsasca, A.; Wielgus, M. Images and photon ring signatures of thick disks around black holes. *Astron. Astrophys.* **2022**, *667*, A170. [CrossRef]

64. Ricarte, A.; Johnson, M.D.; Kovalev, Y.Y.; Palumbo, D.C.M.; Emami, R. How Spatially Resolved Polarimetry Informs Black Hole Accretion Flow Models. *Galaxies* **2023**, *11*, 5. [CrossRef]

65. Balbus, S.A.; Hawley, J.F. A powerful local shear instability in weakly magnetized disks. I—Linear analysis. II—Nonlinear evolution. *Astrophys. J.* **1991**, *376*, 214–233. [CrossRef]

66. Mahadevan, R. Scaling Laws for Advection-dominated Flows: Applications to Low-Luminosity Galactic Nuclei. *Astrophys. J.* **1997**, *477*, 585–601. [CrossRef]

67. Kawazura, Y.; Barnes, M.; Schekochihin, A.A. Thermal disequilibration of ions and electrons by collisionless plasma turbulence. *Proc. Natl. Acad. Sci. USA* **2019**, *116*, 771–776. [CrossRef]

68. Howes, G.G. A prescription for the turbulent heating of astrophysical plasmas. *Mon. Not. R. Astron. Soc.* **2010**, *409*, L104–L108. [CrossRef]

69. Ryan, B.R.; Ressler, S.M.; Dolence, J.C.; Gammie, C.; Quataert, E. Two-temperature GRRMHD Simulations of M87. *Astrophys. J.* **2018**, *864*, 126. [CrossRef]

70. Chael, A.; Rowan, M.; Narayan, R.; Johnson, M.; Sironi, L. The role of electron heating physics in images and variability of the Galactic Centre black hole Sagittarius A*. *Mon. Not. R. Astron. Soc.* **2018**, *478*, 5209–5229. [CrossRef]

71. Chael, A.; Narayan, R.; Johnson, M.D. Two-temperature, Magnetically Arrested Disc simulations of the jet from the supermassive black hole in M87. *Mon. Not. R. Astron. Soc.* **2019**, *486*, 2873–2895. [CrossRef]

72. Mizuno, Y.; Fromm, C.M.; Younsi, Z.; Porth, O.; Olivares, H.; Rezzolla, L. Comparison of the ion-to-electron temperature ratio prescription: GRMHD simulations with electron thermodynamics. *Mon. Not. R. Astron. Soc.* **2021**, *506*, 741–758. [CrossRef]

73. Penrose, R. Gravitational Collapse: The Role of General Relativity. *Nuovo C. Riv. Ser.* **1969**, *1*, 252.

74. Prieto, M.A.; Fernández-Ontiveros, J.A.; Markoff, S.; Espada, D.; González-Martín, O. The central parsecs of M87: Jet emission and an elusive accretion disc. *Mon. Not. R. Astron. Soc.* **2016**, *457*, 3801–3816. [CrossRef]

75. Broderick, A.E.; Tiede, P.; Pesce, D.W.; Gold, R. Measuring Spin from Relative Photon-ring Sizes. *Astrophys. J.* **2022**, *927*, 6. [CrossRef]

76. Akiyama, K. et al. [Event Horizon Telescope Collaboration]. First M87 Event Horizon Telescope Results. VIII. Magnetic Field Structure near The Event Horizon. *Astrophys. J. Lett.* **2021**, *910*, L13. [CrossRef]

77. Zamaninasab, M.; Clausen-Brown, E.; Savolainen, T.; Tchekhovskoy, A. Dynamically important magnetic fields near accreting supermassive black holes. *Nature* **2014**, *510*, 126–128. [CrossRef]

78. Gammie, C.F.; McKinney, J.C.; Tóth, G. HARM: A Numerical Scheme for General Relativistic Magnetohydrodynamics. *Astrophys. J.* **2003**, *589*, 444. [CrossRef]

79. Emami, R.; Anantua, R.; Ricarte, A.; Doeleman, S.S.; Broderick, A.; Wong, G.; Blackburn, L.; Wielgus, M.; Narayan, R.; Tremblay, G.; et al. Probing Plasma Composition with the Next Generation Event Horizon Telescope (ngEHT). *Galaxies* **2023**, *11*, 11. [CrossRef]

80. Mertens, F.; Lobanov, A.P.; Walker, R.C.; Hardee, P.E. Kinematics of the jet in M 87 on scales of 100–1000 Schwarzschild radii. *Astron. Astrophys.* **2016**, *595*, A54. [CrossRef]

81. Walker, R.C.; Hardee, P.E.; Davies, F.B.; Ly, C.; Junor, W. The Structure and Dynamics of the Subparsec Jet in M87 Based on 50 VLBA Observations over 17 Years at 43 GHz. *Astrophys. J.* **2018**, *855*, 128. [CrossRef]

82. Komissarov, S.S. Numerical simulations of relativistic magnetized jets. *Mon. Not. R. Astron. Soc.* **1999**, *308*, 1069–1076. [CrossRef]

83. Janssen, M.; Falcke, H.; Kadler, M.; Ros, E.; Wielgus, M.; Akiyama, K.; Baloković, M.; Blackburn, L.; Bouman, K.L.; Chael, A.; et al. Event Horizon Telescope observations of the jet launching and collimation in Centaurus A. *Nat. Astron.* **2021**, *5*, 1017–1028. [CrossRef]

84. Blandford, R.D.; Payne, D.G. Hydromagnetic flows from accretion disks and the production of radio jets. *Mon. Not. R. Astron. Soc.* **1982**, *199*, 883–903. [CrossRef]

85. Wielgus, M. Photon rings of spherically symmetric black holes and robust tests of non-Kerr metrics. *Phys. Rev. D* **2021**, *104*, 124058. [CrossRef]

86. Raymond, A.W.; Palumbo, D.; Paine, S.N.; Blackburn, L.; Córdova Rosado, R.; Doeleman, S.S.; Farah, J.R.; Johnson, M.D.; Roelofs, F.; Tilanus, R.P.J.; et al. Evaluation of New Submillimeter VLBI Sites for the Event Horizon Telescope. *Astrophys. J. Suppl. Ser.* **2021**, *253*, 5. [CrossRef]

87. Gelaro, R.; McCarty, W.; Suárez, M.J.; Todling, R.; Molod, A.; Takacs, L.; Randles, C.A.; Darmenov, A.; Bosilovich, M.G.; Reichle, R.; et al. The Modern-Era Retrospective Analysis for Research and Applications, Version 2 (MERRA-2). *J. Clim.* **2017**, *30*, 5419–5454. [CrossRef]

88. Salby, M.L. *Fundamentals of Atmospheric Physics*; Academic Press: Cambridge, MA, USA, 1996.

89. Chael, A.A.; Johnson, M.D.; Narayan, R.; Doeleman, S.S.; Wardle, J.F.C.; Bouman, K.L. High-resolution Linear Polarimetric Imaging for the Event Horizon Telescope. *Astrophys. J.* **2016**, *829*, 11. [CrossRef]

90. Chael, A.A.; Johnson, M.D.; Bouman, K.L.; Blackburn, L.L.; Akiyama, K.; Narayan, R. Interferometric Imaging Directly with Closure Phases and Closure Amplitudes. *Astrophys. J.* **2018**, *857*, 23. [CrossRef]

91. Thompson, A.R.; Moran, J.M.; Swenson, G.W., Jr. *Interferometry and Synthesis in Radio Astronomy*, 3rd ed.; Springer: Berlin/Heidelberg, Germany, 2017. [CrossRef]

92. Paine, S. *The Am Atmospheric Model*; Zenodo: Geneva, Switzerland, 2019. [CrossRef]

93. Blackburn, L.; Chan, C.k.; Crew, G.B.; Fish, V.L.; Issaoun, S.; Johnson, M.D.; Wielgus, M.; Akiyama, K.; Barrett, J.; Bouman, K.L.; et al. EHT-HOPS Pipeline for Millimeter VLBI Data Reduction. *Astrophys. J.* **2019**, *882*, 23. [CrossRef]

94. Rioja, M.J.; Dodson, R. Precise radio astrometry and new developments for the next-generation of instruments. *Astron. Astrophys. Rev.* **2020**, *28*, 6. [CrossRef]

95. Palumbo, D.C.M.; Doeleman, S.S.; Johnson, M.D.; Bouman, K.L.; Chael, A.A. Metrics and Motivations for Earth-Space VLBI: Time-resolving Sgr A* with the Event Horizon Telescope. *Astrophys. J.* **2019**, *881*, 62. [CrossRef]

96. Wielgus, M.; Akiyama, K.; Blackburn, L.; Chan, C.k.; Dexter, J.; Doeleman, S.S.; Fish, V.L.; Issaoun, S.; Johnson, M.D.; Krichbaum, T.P.; et al. Monitoring the Morphology of M87* in 2009–2017 with the Event Horizon Telescope. *Astrophys. J.* **2020**, *901*, 67. [CrossRef]

97. Kim, J.Y.; Krichbaum, T.P.; Broderick, A.E.; Wielgus, M.; Blackburn, L.; Gómez, J.L.; Johnson, M.D.; Bouman, K.L.; Chael, A.; Akiyama, K.; et al. Event Horizon Telescope imaging of the archetypal blazar 3C 279 at an extreme 20 microarcsecond resolution. *Astron. Astrophys.* **2020**, *640*, A69. [CrossRef]

98. Issaoun, S.; Wielgus, M.; Jorstad, S.; Krichbaum, T.P.; Blackburn, L.; Janssen, M.; Chan, C.k.; Pesce, D.W.; Gómez, J.L.; Akiyama, K.; et al. Resolving the Inner Parsec of the Blazar J1924-2914 with the Event Horizon Telescope. *Astrophys. J.* **2022**, *934*, 145. [CrossRef]

99. Jorstad, S.; Wielgus, M.; Lico, R.; Issaoun, S.; Broderick, A.E.; Pesce, D.W.; Liu, J.; Zhao, G.Y.; Krichbaum, T.P.; Blackburn, L.; et al. The Event Horizon Telescope Image of the Quasar NRAO 530. *Astrophys. J.* **2023**, *943*, 170. [CrossRef]

100. EHT MWL Science Working Group; Algaba, J.C.; Anczarski, J.; Asada, K.; Baloković, M.; Chandra, S.; Cui, Y.Z.; Falcone, A.D.; Giroletti, M.; Goddi, C.; et al. Broadband Multi-wavelength Properties of M87 during the 2017 Event Horizon Telescope Campaign. *Astrophys. J. Lett.* **2021**, *911*, L11. [CrossRef]

101. Deller, A.T.; Brisken, W.F.; Phillips, C.J.; Morgan, J.; Alef, W.; Cappallo, R.; Middelberg, E.; Romney, J.; Rottmann, H.; Tingay, S.J.; et al. DiFX-2: A More Flexible, Efficient, Robust, and Powerful Software Correlator. *Publ. Astron. Soc. Pac.* **2011**, *123*, 275. [CrossRef]

102. Vázquez, A.J.; Elosegui, P.; Lonsdale, C.J.; Crew, G.B.; Fish, V.L.; Ruszczyk, C.A. Model-based Performance Characterization of Software Correlators for Radio Interferometer Arrays. *Publ. Astron. Soc. Pac.* **2022**, *134*, 104501. [CrossRef]

103. Janssen, M.; Goddi, C.; van Bemmel, I.M.; Kettenis, M.; Small, D.; Liuzzo, E.; Rygl, K.; Martí-Vidal, I.; Blackburn, L.; Wielgus, M.; et al. rPICARD: A CASA-based calibration pipeline for VLBI data. Calibration and imaging of 7 mm VLBA observations of the AGN jet in M 87. *Astron. Astrophys.* **2019**, *626*, A75. [CrossRef]

104. Broderick, A.E.; Gold, R.; Karami, M.; Preciado-López, J.A.; Tiede, P.; Pu, H.Y.; Akiyama, K.; Alberdi, A.; Alef, W.; Asada, K.; et al. THEMIS: A Parameter Estimation Framework for the Event Horizon Telescope. *Astrophys. J.* **2020**, *897*, 139. [CrossRef]

105. Pesce, D.W. A D-term Modeling Code (DMC) for Simultaneous Calibration and Full-Stokes Imaging of Very Long Baseline Interferometric Data. *Astron. J.* **2021**, *161*, 178. [CrossRef]

106. Phillips, C.; Whitney, A.; Sekido, M.; Kettenis, M. *VTP: VDIF Transport Protocol*; Technical Report; Istituto di Radioastronomia: Bologna, Italy, 2012.

107. Whitney, A.R.; Beaudoin, C.J.; Cappallo, R.J.; Corey, B.E.; Crew, G.B.; Doeleman, S.S.; Lapsley, D.E.; Hinton, A.A.; McWhirter, S.R.; Niell, A.E.; et al. Demonstration of a 16 Gbps Station^{-1} Broadband-RF VLBI System. *Publ. Astron. Soc. Pac.* **2013**, *125*, 196. [CrossRef]